Seismic Actions on Long Tunnels: Records from 1-g Shaking Table Tests

Yong Yuan[1,2]

1. College of Civil Engineering, Tongji University, Shanghai 200092, China
2. State Key Laboratory for Disaster Reduction in Civil Engineering, Tongji University, Shanghai 200092, China

Correspondence
Yong Yuan, yuany@tongji.edu.cn

Funding Information
This research is supported by the National Natural Science Foundation of China (NSFC 52061135112).

Abstract

This paper presents the current research progress in long tunnels subjected to earthquakes. Using the facilities of the multi-functional laboratory of the state-key laboratory, a series of large-scale shaking table tests were completed considering long tunnels under the excitation of travelling waves or junction structures, ground variations, tunnels crossing liquefiable ground, and fault sites under strong shaking. The test results were compared with numerical and analytical calculations to help understand this sophisticated problem. Several meaningful records can be used for the aseismic design of long tunnels and validation of the design formula.

Key words: tunnel; travelling wave; variation of structure; site condition; liquefiable ground; fault; shaking table test

1. Introduction

The seismic design of underground structures enhances their resistance to damage during strong earthquakes[1–3]. Significant progress has been made in the past three decades to understand the seismic behavior of tunnels both experimentally and theoretically[4].

Three types of seismic actions are enforced on tunnels (or underground structures), as identified in the review by John and Zahrah[1]. Specifically, (1) shaking deformation induced by strata vibration, (2) ground failures such as landslides or soil liquefaction, and (3) fault dislocation triggered by an earthquake.

The understanding of the seismic deformation gives analytical solution of ground deformation upon on tunnel. Most solutions, such as analytical analysis of elastic wave propagation and numerical simulation of vibration, can be verified under the transverse excitation of shaking table tests[4]. In this manner, a simplified approach can be applied to aseismic design, as documented by guidelines and codes[5]. The cross-sectional response of a tunnel is an idealized case of uniform excitation from a rigid bedrock. A long tunnel crosses sophisticated strata, as shown in Fig. 1, partially in rock strata that cross faults, soft ground, and even sand deposits that liquefy during strong earthquakes. However, these aspects have not been studied in detail.

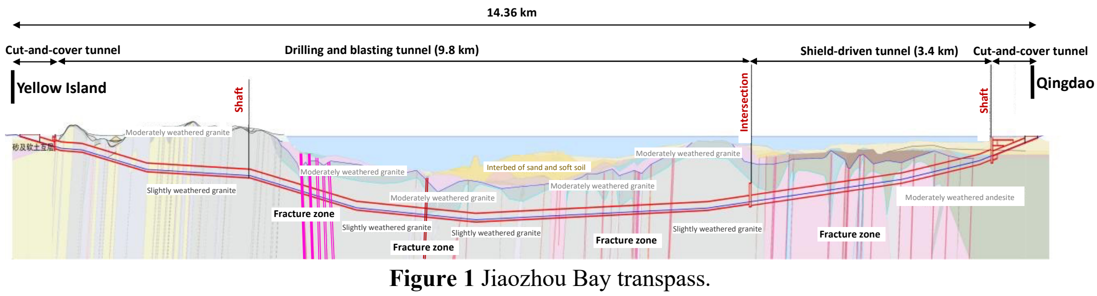

Figure 1 Jiaozhou Bay transpass.

This paper presents a study on the three main actions of long tunnels with intensive 1-g shaking table tests, partially in contrast to analytical or numerical analysis of ground shaking deformation. The effects of discrepancy displacement owing to travelling waves, ground variations, and variation of stiffness of the tunnel were stressed correspondingly for the ground vibration action on the long tunnel. The action of ground liquefaction on the tunnel uplift was investigated in contrast to the free-field response, both on initial liquefaction and multiple shaking. Furthermore, experiments on tunnel-crossing faults have revealed a distinct dynamic response between the footwall and hanging wall.

2. Deformation during earthquakes

2.1 Response under travelling wave

Long tunnels suffer non-uniform excitation of travelling waves even in uniform media if the length of the tunnel is significantly larger than the wavelength of seismic propagation in the medium. Theoretical analysis of the displacement response of uniform ground during shaking was proposed by Newmark[6] and Kuesel[7]. Free-field analysis ensures that the seismic excitation is of the form of a sinusoidal function at a critical incident angle with respect to the axial direction of the tunnel. A simplified analytical solution of the tunnel as an elastic beam subjected to the displacement of free-field ground was deduced[1–3]. Theoretically, the displacement responses of the tunnel can be obtained by solving the following differential equations

$$\begin{cases} EI\dfrac{d^4v(x)}{dx^4} + k_\mathrm{t}v(x) = k_\mathrm{t}v_\mathrm{G}(x) \\ EA\dfrac{d^2u(x)}{dx^2} - k_\mathrm{a}u(x) = -k_\mathrm{a}u_\mathrm{G}(x) \end{cases}, \tag{1}$$

where EI and EA are the cross-sectional bending stiffness and axial stiffness per unit length of the tunnel, respectively; k_t and k_a are the vertical (lateral) and horizontal (axial) resistance factors of the foundation, respectively; $v(x)$ and $u(x)$ are the vertical and axial displacements of the tunnel at coordinate x, respectively; and $v_\mathrm{G}(x)$ and $u_\mathrm{G}(x)$ are the vertical and axial displacements of the ground at coordinate x, respectively, under seismic action, as Fig. 2. However, tunnels typically do not have portions, and the assumption of uniform stiffness is impractical. Furthermore, ground variations cause the ground deformation to differ from an idealized sinusoidal formation.

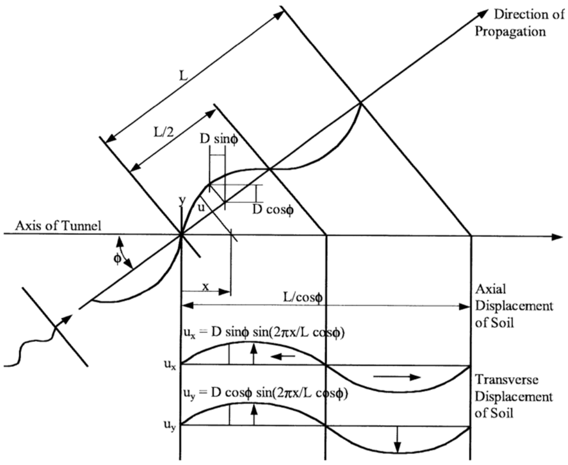

Figure 2 Assumption of deformation action on longitudinal of tunnel.[1–3]

In the recorded ground movement during an earthquake, which is a random process. To obtain the response of a long tunnel under a travelling wave input, a multi-shaking table test is a powerful tool. To transfer discrete vibration inputs from an individual shaking table to the continuous propagation of shear waves in the modelled ground, a system should be implemented using the sound principle. Based on the theory of elastic waves, an analytical solution for the dynamic responses of a tunnel, simplified as a Euler beam, was deduced under an arbitrary loading process[8]. Using this fundamental solution, a testing system with a shaking-table array, as shown in Fig. 3, was set up to simulate a travelling wave[9]. This shaking array system has been successfully applied to immersed tunnels[10] and shield tunnels[11] to study the dynamic responses of long tunnels under travelling waves.

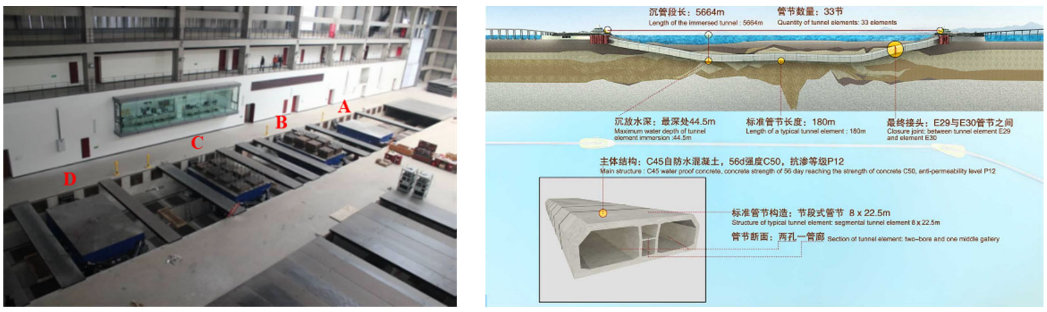

(a) **(b)**

Figure 3 Shaking-table array and testing of immersed tunnel[10] : **(a)** Shaking table array; and **(b)** Segments of HZM immersed tunnel.

2.1.1 Free field responses with shaking table array

As a reference, the dynamic response of a free field (FF) under a travelling wave is of fundamental significance. A scaled FF ground, as shown in Fig.4 (a), with the labels of the accelerometers was designed to test shear wave propagation. The accelerometer was labelled in the manner of "B#-A*-@", where # refers to Box location, * means the direction of input vibration (X-perpendicular to the sectional profile, Y-along the sectional profile), and @ indicates the position (that is, -2 at the middle height, -3 at the surface of the ground), of an accelerometer. The input-excitation cases are listed in Table 1. Here, SH01 means Shanghai synthetical motion as Fig. 4 (b) input from four tables simultaneously, whereas N-SH01 indicates the same motion inputted from the far left to the far right tables in a travelling manner.

The recorded responses of each accelerometer under the inputs SH01 and N-SH01 are shown in Fig. 4 (c). It can be observed that the acceleration response at the surface is dominant with respect to that in the middle of the ground, whether under uniform or nonuniform excitation. Furthermore, the acceleration response of each box at the same position is approximately identical under uniform excitation. This can be observed in the peak acceleration (PA) data for each position listed in Table 2. In contrast, the delayed response in the sequential box is evident, as highlighted by the Fourier spectrum in Table 3. Comparing Table 3 with Table 2, it can be seen that the PA under nonuniform excitation is more prominent with respect to the PA under uniform excitation both at the middle and at the surface. Figure 4 (d) presents the time/frequency spectrum at different locations. The spectrum varies in any domain of the ground, which indicates that the impact of wave superposition varies with space during the propagation of the travelling wave.

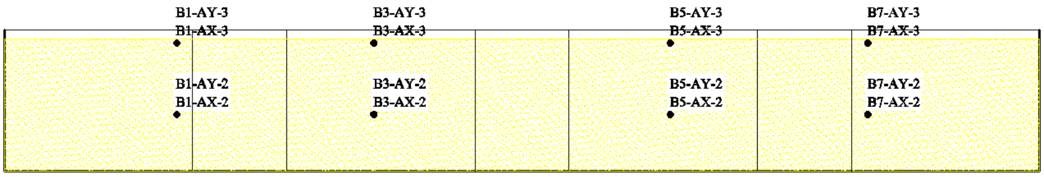

(a)

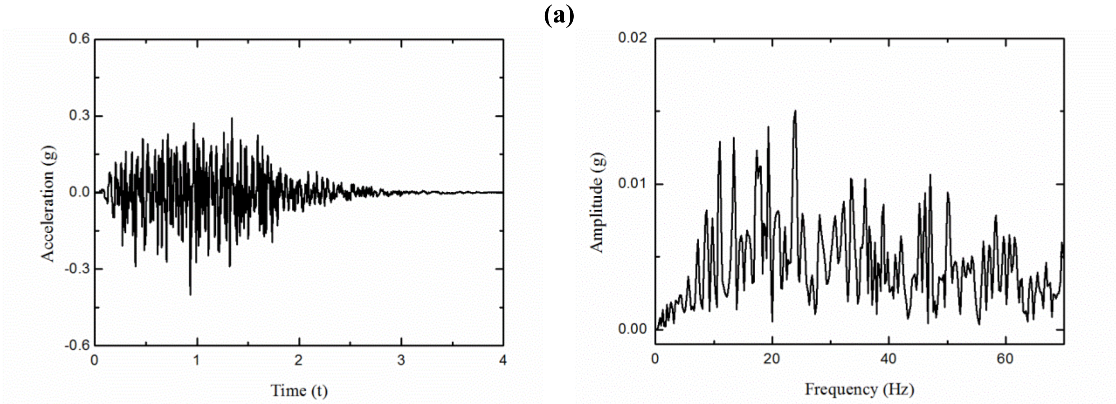

(b)

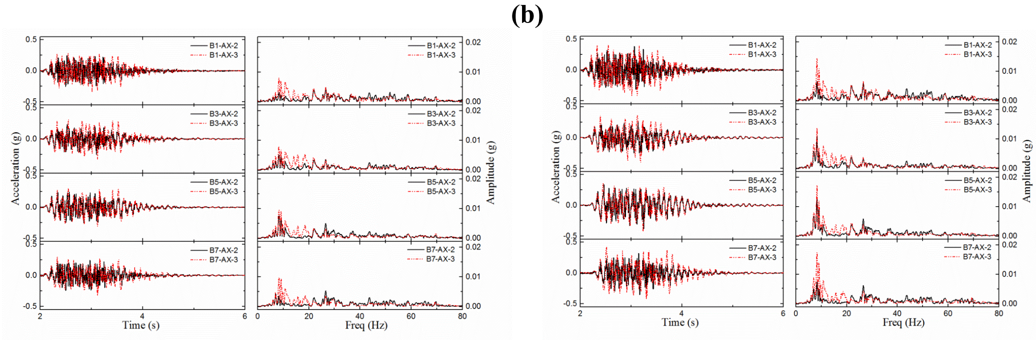

SH01

N-SH01

(c)

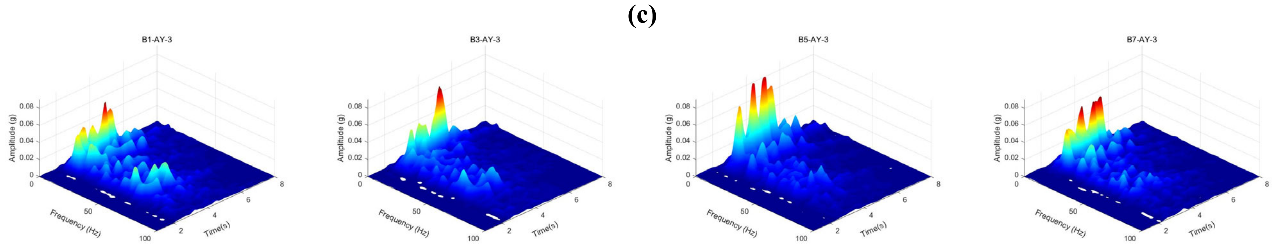

(d)

Figure 4 Site responses under travelling wave: lateral excitation: **(a)** Scale FF ground; **(b)** Shanghai synthetical ground motion; **(c)** Acceleration responses (SH01 and N-SH01); and **(d)** Time/Frequency Spectrum: N-SH04.

Table 1 Loading cases of shaking table tests: FF.

Input cases	SH01/N-SH01	SH02//N-SH02	SH03//N-SH03	SH04//N-SH04
Reference period(yr)	50	50	100	100
Probability of exceedance	10%	3%	10%	3%
PGA (g)	0.3	0.4	0.35	0.47
Predominate Frequency（Hz）	26.6	26.6	34.9	34.9

Table 2 Peak acceleration response at each position (SH01).

SH01		B1	B3	B5	B7
PA (g)	Inner	-0.256	-0.246	-0.250	0.244
	Surface	-0.338	-0.327	-0.322	-0.325
t_p (s)	Inner	2.496	3.098	2.852	2.973
	Surface	3.016	3.121	3.117	3.121

Table 3 Peak acceleration response at each position (N-SH01).

N-SH01		B1	B3	B5	B7
PA (g)	Inner	0.38	0.27	-0.38	-0.35
	Surface	-0.43	-0.42	-0.42	-0.42
t_p (s)	Inner	3.07	3.14	3.25	3.17
	Surface	3.12	3.19	3.24	3.30

2.1.2 Slope site

A slope site was modeled based on the prototype of the immersed tunnel of the Hong Kong–Zhuhai–Macau Bridge (HZM). Figures 5(a) and (b) show the slope site and the layout of the sensors, respectively. Table 4 lists the uniform and non-uniform excitations in the travelling mode, both with a peak ground acceleration (PGA) of 0.25 g. In Case DZ1, white noise was input to verify that the scaled ground model satisfied the similarity requirements. The acceleration responses observed at DZ2 and DZ3 are shown in Fig. 5(c). Compared with the test results gathered from Case DZ2, it is evident that the acceleration responses at each measuring point display significant discrepancies under non-uniform excitation in Case DZ3.

Table 4 Loading cases of slope site.

Cases	PGA（g）	Motion	Excitation	Direction of vibration
DZ1	0.1	White noise	Uniform	Two ways
DZ2	0.25	Artificial motion	Uniform	Lateral
DZ3	0.25	Artificial motion	Non-uniform	Lateral (M2→M11)

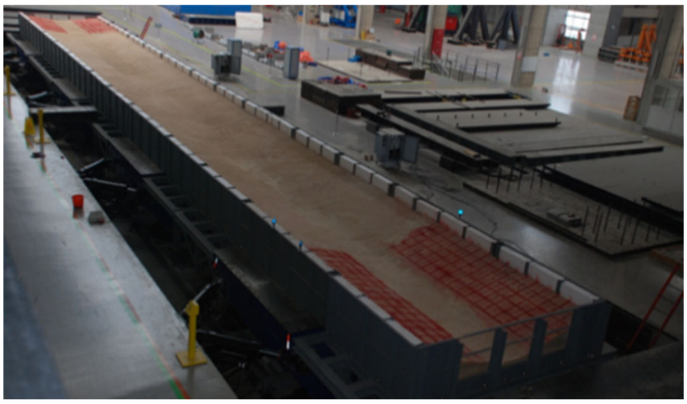

(a)

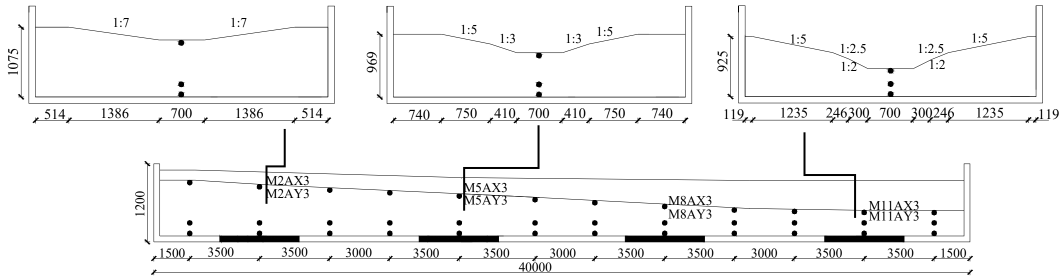

(b)

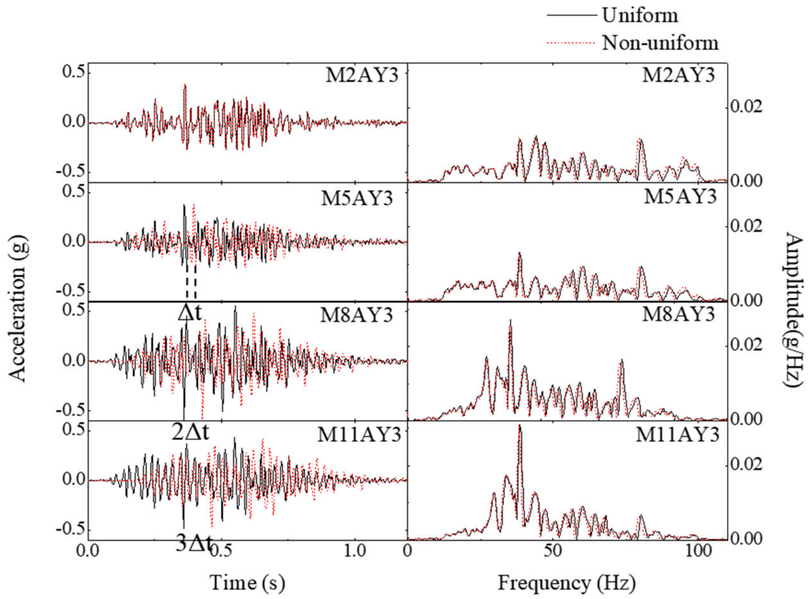

(c)

Figure 5 Response of slope site : DZ2-uniform excitation and DZ3-travelling wave: **(a)** Slope site; **(b)** Layout of sensors; and **(c)** Acceleration responses: time histories and Fourier spectrum.

2.1.3 Response of immersed tunnel

The scaled immersed tunnel was tested at the same slope site as described in Section 2.1.2, as shown in Fig. 6(a). This section presents the results for loading cases C01 and C02 under transverse excitation. The input artificial waves lasts 1.6 s, with a PGA of 0.25 g. Case C01 was subjected to uniform excitation, while case C02 experienced non-uniform excitation. Fig. 6(b) shows the sensor layout.

Figure 6(c) shows the acceleration responses of the tunnel and nearby sites under the C01 excitation. The results indicate that the peak responses of the tunnel are more pronounced than those of the surrounding soil, although they occur almost simultaneously in terms of the time histories and spectra. In the high-frequency domain, the tunnel played a dominant role in the interaction with the surrounding soil.

A comparison of the time histories and spectra of the acceleration between C01 and C02, as shown in Fig. 6(d), reveals no significant differences. However, the lateral displacement of the tunnel within the initial 0.15 s shows a clear distinction, as illustrated in Fig. 6(e). For C01, the tunnel moved nearly simultaneously toward one side. By contrast, the lateral displacement began with one tunnel section and propagated sequentially to the other sections in C02. Furthermore, the magnitude of the displacement in C02 was significantly larger, as depicted in Fig. 6(f). Joint dislocation occurred in a propagative manner, reaching the far end, even during the initial shaking period. This highlights the importance of accounting for nonuniform excitation in the seismic design of long tunnels.

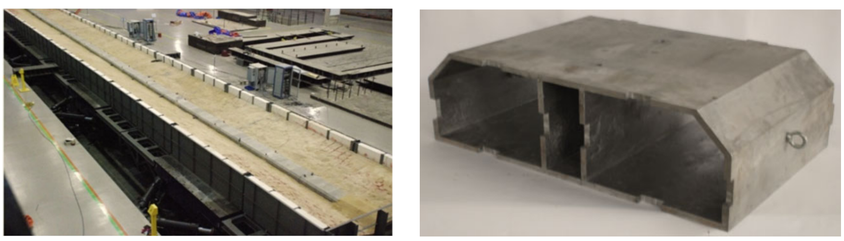

(a)

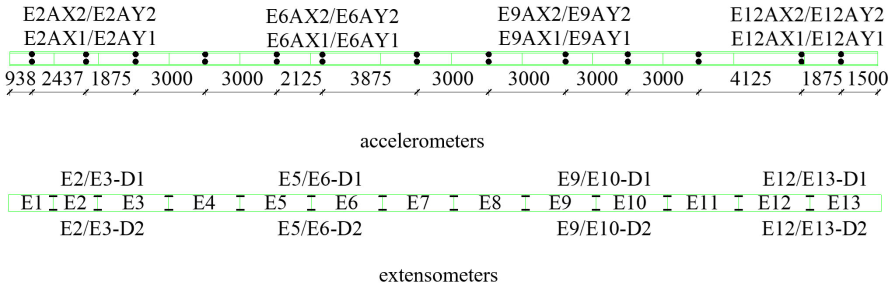
E2AX2/E2AY2
E2AX1/E2AY1
E6AX2/E6AY2
E6AX1/E6AY1
E9AX2/E9AY2
E9AX1/E9AY1
E12AX2/E12AY2
E12AX1/E12AY1
938 2437 1875 3000 3000 2125 3875 3000 3000 3000 3000 4125 1875 1500
accelerometers
E2/E3-D1
E5/E6-D1
E9/E10-D1
E12/E13-D1
E1 E2 E3 E4 E5 E6 E7 E8 E9 E10 E11 E12 E13
E2/E3-D2
E5/E6-D2
E9/E10-D2
E12/E13-D2
extensometers

(b)

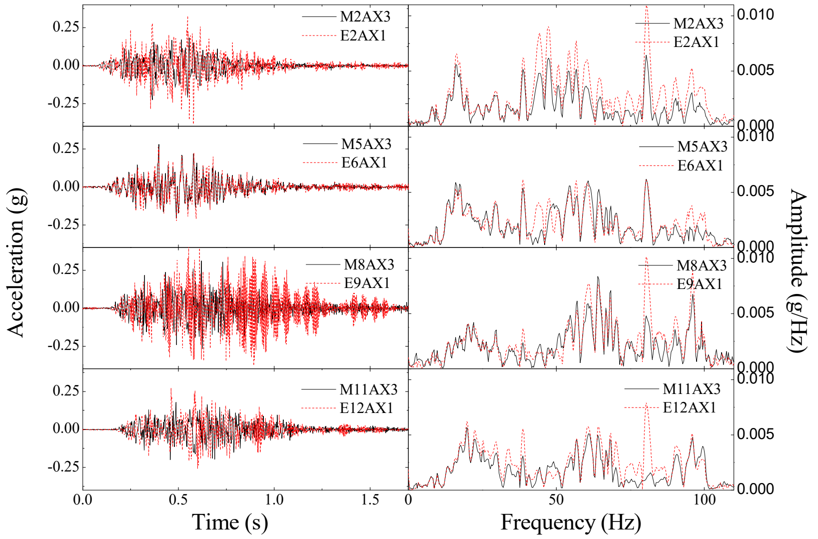
M2AX3
E2AX1
M5AX3
E6AX1
M8AX3
E9AX1
M11AX3
E12AX1
Acceleration (g)
Amplitude (g/Hz)
Time (s)
Frequency (Hz)

(c)

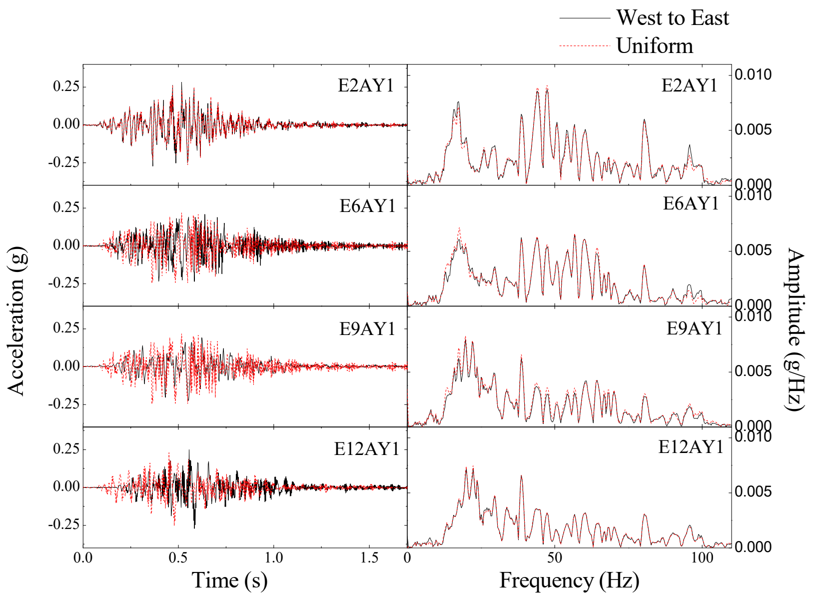
West to East
Uniform
E2AY1
E6AY1
E9AY1
E12AY1
Acceleration (g)
Amplitude (g/Hz)
Time (s)
Frequency (Hz)

(d)

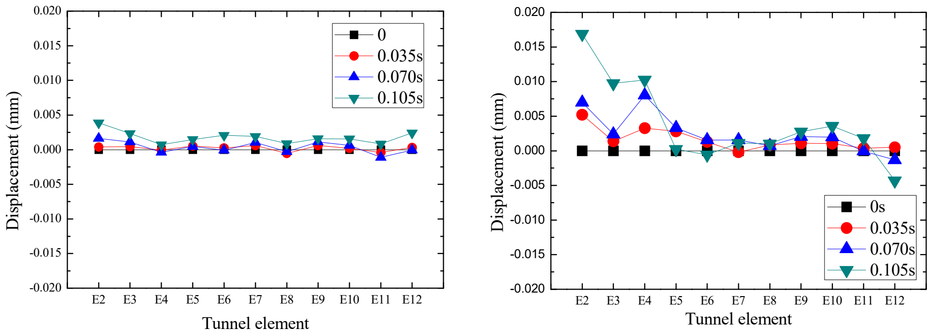

Case C01 Case C02

(e)

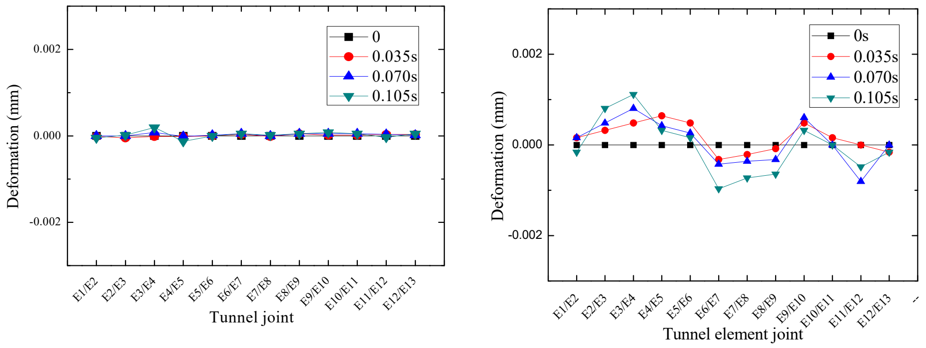

Case C01 Case C02

(f)

Figure 6 Dynamic responses of immersed tunnel: lateral excitation: **(a)** Scaled immersed tunnel; **(b)** Location of accelerometers and joint extensometers; **(c)** Case C01: Structure (red dot line, E); Soil (black line, M); **(d)** Structure: C01 (Uniform, dot line); C02 (Non-uniform: west to east, black line); **(e)** Lateral displacement (Case C01 and C02); and **(f)** Joint extension/closure (Case C01 and C02).

2.2 Discrepant Responses due to Structural Variation

A long tunnel presents discrepant responses even under uniform excitation under varying structural stiffness at a specified portion. As shown in Fig. 7(a), a large-scale shaking-table test was conducted on the conjunction structures between the shaft and tunnels and the connecting passageway between the two lanes of the tunnels[12–14]. Table 5 lists the primary test cases. The input excitations were similar to those used in the immersed tunnel, whose amplitudes were scaled up according to similitude relations. The table was shaken horizontally in the transverse and longitudinal directions of the tunnel. As illustrated in Fig. 7(b), the model of the conjunction structures was positioned at the longitudinal centerline of the container and buried at a depth of 385 mm. The following content of the subsection mainly focuses on the shaft-tunnel junction.

Table 5 Loading cases of shaking table tests: conjunction structures.

Input cases	M1	M2	M3	M4
Reference period (yr)	50	50	50	50
Probability of exceedance	10%	3%	10%	3%
PGA (g)	0.3	0.4	0.3	0.4
Predominate frequency (Hz)	26.6	23.9	26.6	23.9
Shaking direction	Transverse	Transverse	Longitudinal	Longitudinal

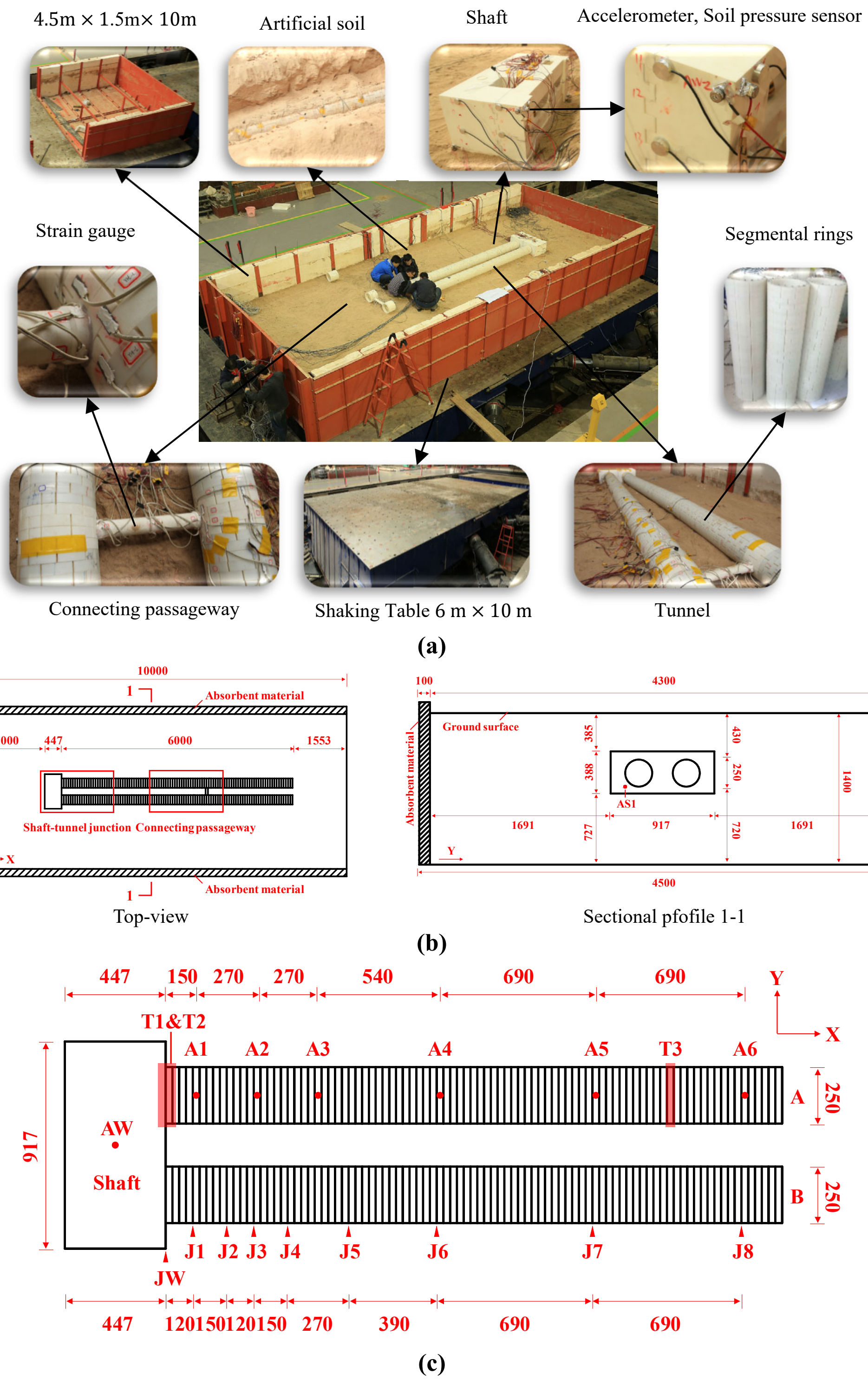
4.5m × 1.5m× 10m
Artificial soil
Shaft
Accelerometer, Soil pressure sensor
Strain gauge
Segmental rings
Connecting passageway
Shaking Table 6 m × 10 m
Tunnel
(a)
10000
Absorbent material
2000
447
6000
1553
4500
Shaft-tunnel junction
Connecting passageway
Y
X
1
Top-view
100
4300
100
Ground surface
385
388
430
250
AS1
1400
1500
1691
917
1691
727
720
Absorbent material
4500
Sectional pfofile 1-1
(b)
447
150
270
270
540
690
690
T1&T2
A1
A2
A3
A4
A5
T3
A6
AW
Shaft
917
A
B
250
250
J1
J2
J3
J4
J5
J6
J7
J8
JW
447
120150120150
270
390
690
690
(c)

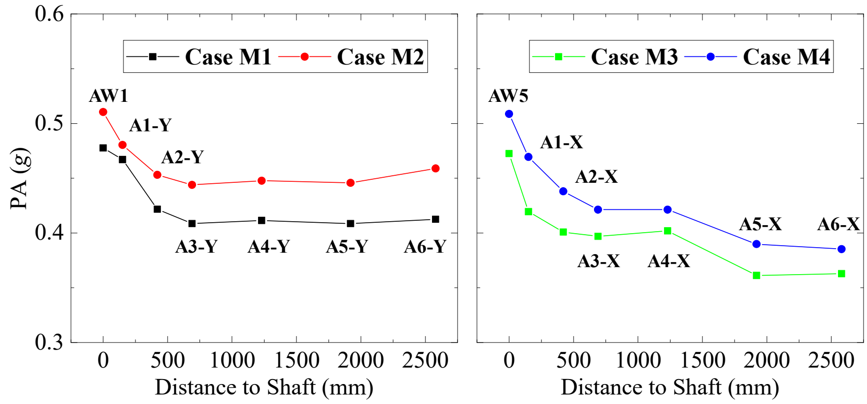

(d)

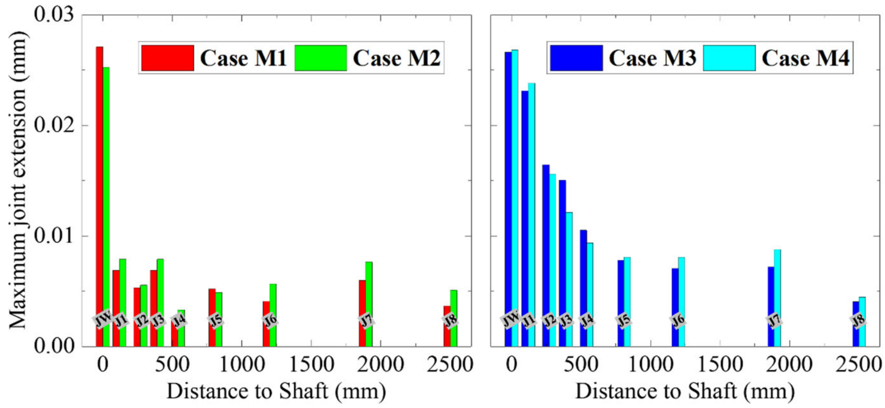

(e)

Figure 7 Discrepant responses due to structural variation: experiments: **(a)** Set-up of model testing; **(b)** Layout of the conjunction model (unit: mm); **(c)** Positions of sensors: accelerometers and joint extensometers; **(d)** Peak accelerations of the shaft-tunnel junction; **(e)** Maximum joint extensions of the shaft-tunnel junction.

2.2.1 Discrepant responses of the tunnel

The model of the shaft-tunnel junction was heavily instrumented, as shown in Fig. 7 (c), where A # denotes the number of accelerometers used and J denotes the number of joint extensometers. Discrepant responses were immediately observed in the acceleration data. The peak accelerations recorded by the accelerometers are presented in Fig. 7(d). In both the transverse and longitudinal shaking cases, the shaft was more sensitive to the input motion; therefore, it always exhibited the largest peak acceleration. As the distance from the shaft increased, the recorded peak acceleration decreased. The consequence of the discrepant accelerations is seen in the joint extension, which is similarly plotted in Fig. 7 (e). As expected, the deformation was the largest at the connection of the shaft and tunnels, that is, JW, where the discrepancy in acceleration was the most acute. For example, in Case M3, the extension at JW was approximately seven times that at J8.

2.2.2 Dynamic analytical model of shaft-tunnel junction

The test data of the joint extension can be interpreted using the classic beam-spring model for the tunnel. The deformation mode for transverse shaking is shown in Fig. 8(a). The tunnel was primarily subjected to a longitudinal bending deformation caused by its differential displacement relative to the shaft. Although this pseudo-static model can predict the deformation of joint extensions with reasonable accuracy, it is inherently flawed because a) it neglects the dynamic soil-structure interaction and b) the shaft-tunnel relative displacement is used as a known factor, which is impossible in real applications. To overcome these flaws of the pseudo-static model, a more advanced dynamic analytical model was developed for the shaft-tunnel junction[15–18]. As shown in Fig. 8(b), the tunnel was simplified into a continuous Euler-Bernoulli beam, and the shaft was regarded as a rigid body. This implies that the shaft must be sufficiently stiff to ignore the deformation. The surrounding soil is represented by a series of springs and dashpots supporting the shaft and tunnel at one end and transmitting seismic motion at the other end. Thus, the dynamic soil-structure interaction is mediated by springs and dashpots. In particular, the coefficients of the springs and dashpots on the shaft were determined using the foundation impedances for rigid caissons proposed by Gazetas[19]. An equation can then be written for the shaft in the frequency domain in the form of

$$\left(\tilde{\mathbf{K}} - \omega^2\mathbf{M} + \mathbf{T}\right)\mathbf{u} = \mathbf{P} + \mathbf{P}_{\mathrm{T}}, \tag{2}$$

where $\tilde{\mathbf{K}}$ is the complex stiffness matrix of the foundation; ω is the angular frequency of the excitation; $\mathbf{M}$ is the mass matrix of the shaft; $\mathbf{T}$ is the additional stiffness matrix of the tunnel; $\mathbf{u}$ is the generalized unknown displacement vector of the shaft; $\mathbf{P}$ is the external loading vector caused by the seismic excitation; $\mathbf{P}_{\mathrm{T}}$ is the additional external loading vector caused by the tunnel. Generally, the $\tilde{\mathbf{K}}$ term, that is the stiffness of the surrounding ground, plays a dominant role. The $\mathbf{P}_{\mathrm{T}}$ term is negligible; therefore, the tunnel primarily affects the shaft as an additional constraint via the $\mathbf{T}$ term. Once the displacements of the shaft are solved using this equation, the responses of the tunnel can be readily obtained using the dynamic beam-spring theory.

To validate the proposed analytical solutions, a 3-dimensional finite element model of a shaft-tunnel junction subjected to vertically propagating shear waves was constructed and computed, as shown in Fig. 8(c). The responses of the shaft-tunnel junction under the same conditions were calculated using the analytical solutions. As demonstrated by the comparisons in Figs. 8(d) and (e), the newly proposed analytical solutions yielded satisfactory results for the displacements of the shaft and the internal forces of the tunnel.

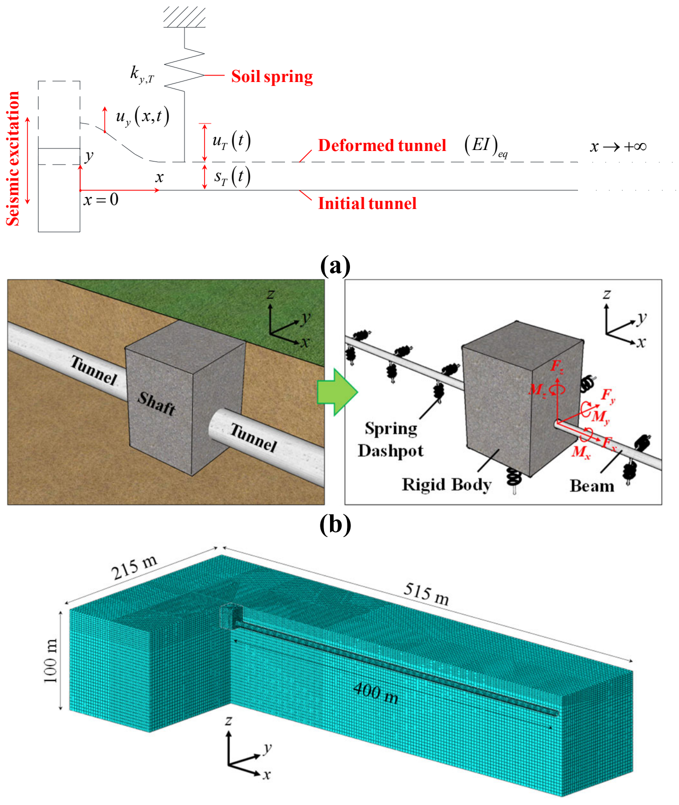

(c)

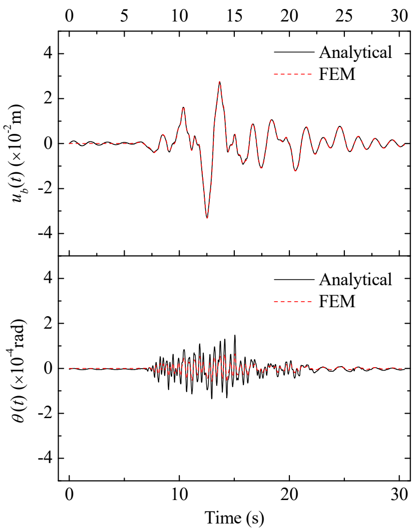

(d)

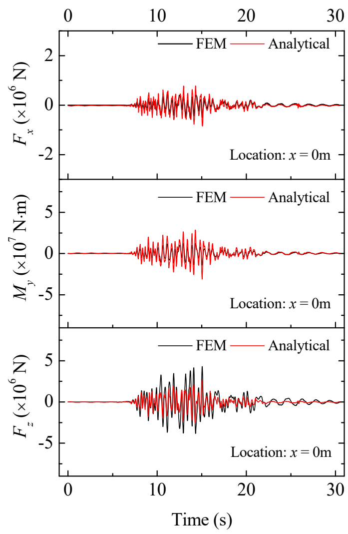

(e)

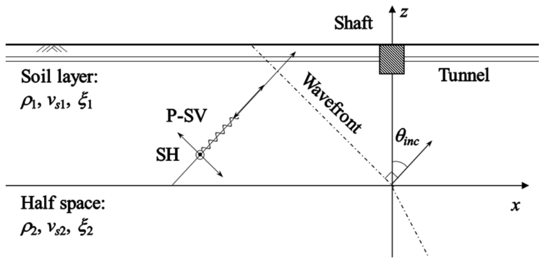

(f)

Figure 8 Discrepant responses due to structural variation: analytical models: **(a)** Pseudo-static model of shaft-tunnel junction subject to transverse shaking; **(b)** Dynamic analytical model of shaft-tunnel junction.; **(c)** Finite element model for the validation of the proposed analytical solutions; **(d)** Translational and rotational displacements of the shaft; **(e)** Internal forces at the connecting point; and **(f)** Dynamic analytical model of shaft-tunnel junction subject to inclined plane wave.

2.2.3 Incorporation of travelling-wave effect

It has been extensively discussed in the previous subsection that non-uniform excitation is a major source of seismic deformation in long tunnels. It is possible that a critical conjunction structure such as a shaft-tunnel junction is subject to this type of seismic impact. As a special case of nonuniform excitation, the traveling wave effect of an inclined plane wave was incorporated into the dynamic analytical model of the shaft-tunnel junction[20,21].

As illustrated in Fig. 8(f), the seismic motion was input in the form of inclined plane P-SV or SH waves. The ground was modeled using a viscoelastic soil layer resting on the underlying half-space. The tunnel axis is oriented in the direction of the horizontal wave propagation such that the traveling wave effect is most prominent in the tunnel. The spatial displacement field is calculated using the stiffness matrix method for layered media[22]. The equation for the displacement of the shaft remains the same as Eq. (2), only external loading vectors $\mathbf{P}$ and $\mathbf{P}_T$ depend on the displacement field of the travelling wave. The solutions were also validated by the results of 3-dimensional numerical computations, similar to those shown in Figs. 8(a), (b), and (c).

Because the shaft generally has limited dimensions, it is less affected by the traveling wave effect. In contrast, the displacements of the tunnel are the superpositions of the shaft displacements and the ground displacement. The influence of the shaft decreased exponentially as the distance from the shaft increased. When the distance is sufficiently large, the response of the tunnel is dominated by the propagation of the travelling wave.

2.3 Variation of Strata

A long tunnel expresses discrepant responses at the location where it crosses the strata, with significant differences in geological deposits. Fig. 9 shows the test results for the tunnels crossing the soil-rock interface. This typical seismic scenario was simulated using a large-scale shaking table test considering the relative stiffness of the ground tunnel as the dominant factor. Accordingly, a refined segmental lining was designed to mimic the structural features of the prototype shield-driven tunnel. Transverse and longitudinal excitations, including artificial, real, and sinusoidal waves, were applied. Initially, the local site effect was analyzed using a free-field model to characterize spatial site conditions.

The resulting discrepant responses of the embedded tunnels were examined. The following section presents an analytical method for addressing the combined effects of variations on both site and structure.

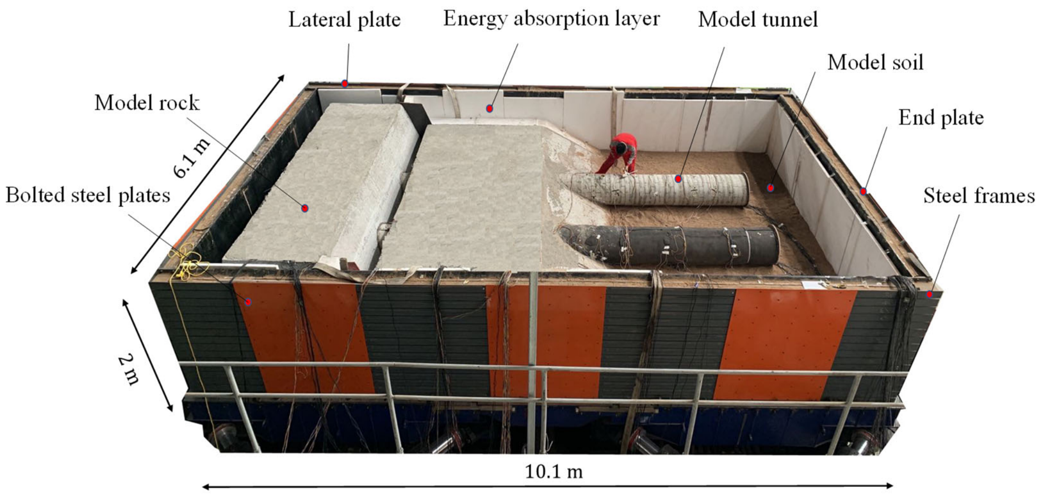

Figure 9 Shaking table test of tunnel crossing soil-rock interface.

The dynamic responses of the tunnel in the soil-rock strata were studied according to the instrument scheme, as shown in Fig. 10. There are 15 accelerometers aligned as a matrix in the vertical longitudinal center plane, namely, AS1–AS15 in Profile 1-1. A0 was attached to the shaking table to record the actual output. The twin tunnels were placed symmetrically in the soil-rock strata, with a clear spacing of 1 m and buried depth of 0.7 m. Three types of sensors were used in the model tunnel. Six accelerometers, numbered A1–A6, were installed at the bottom of the model tunnel. Linear variable displacement transducers were arranged on six lining rings, labelled D1–D6, to monitor the sectional deformation along four diametral directions. The extensions of the eight circumferential joints were also measured using displacement gauges J1 to J8. The following discussion mainly focuses on cases of transverse sinusoidal excitation.

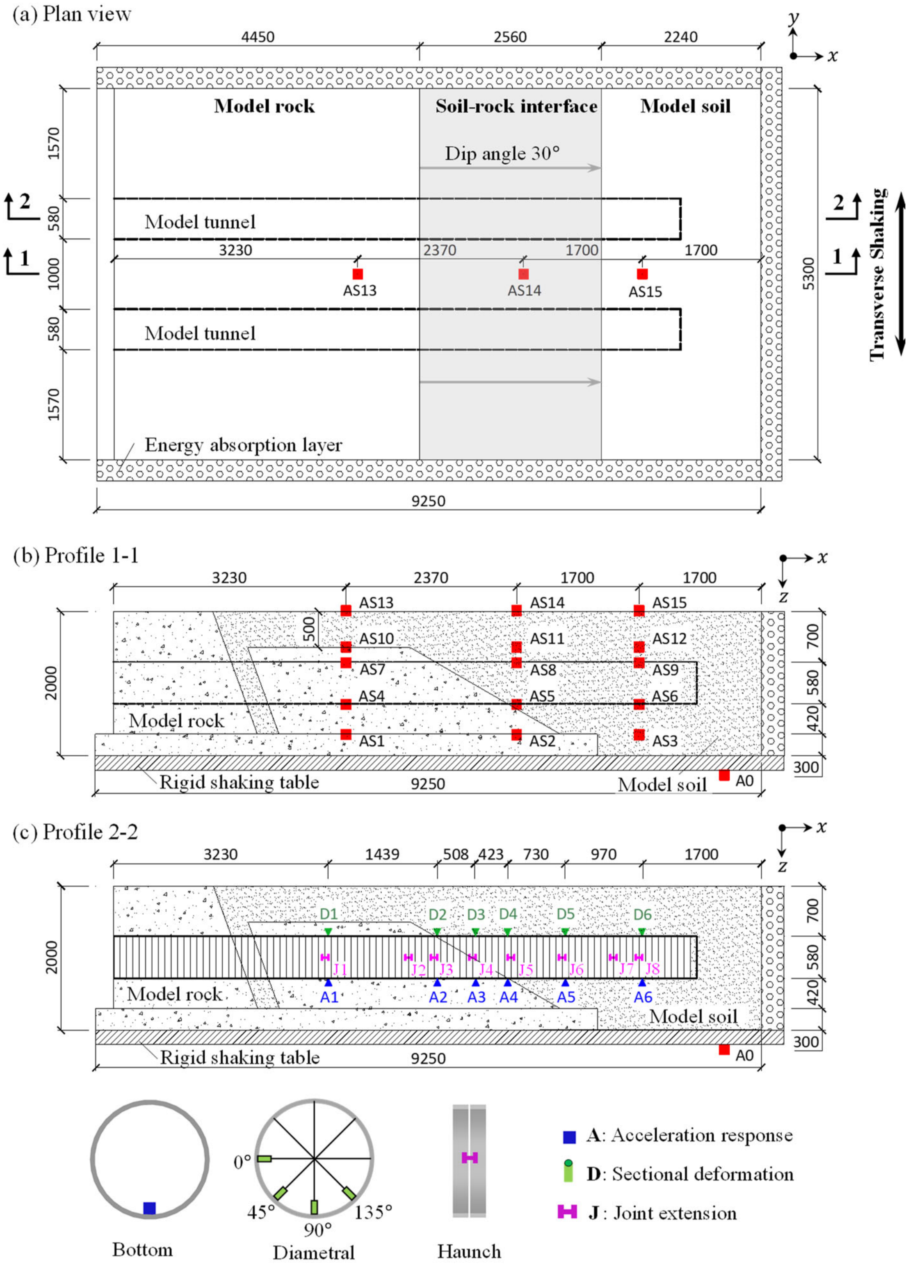

Figure 10 Instruments on the ground-tunnel model: **(a)** plan view; **(b)** Profile 1-1: sensors in the model ground; and **(c)** Profile 2-2: sensors on the model tunnel (Unit: mm).

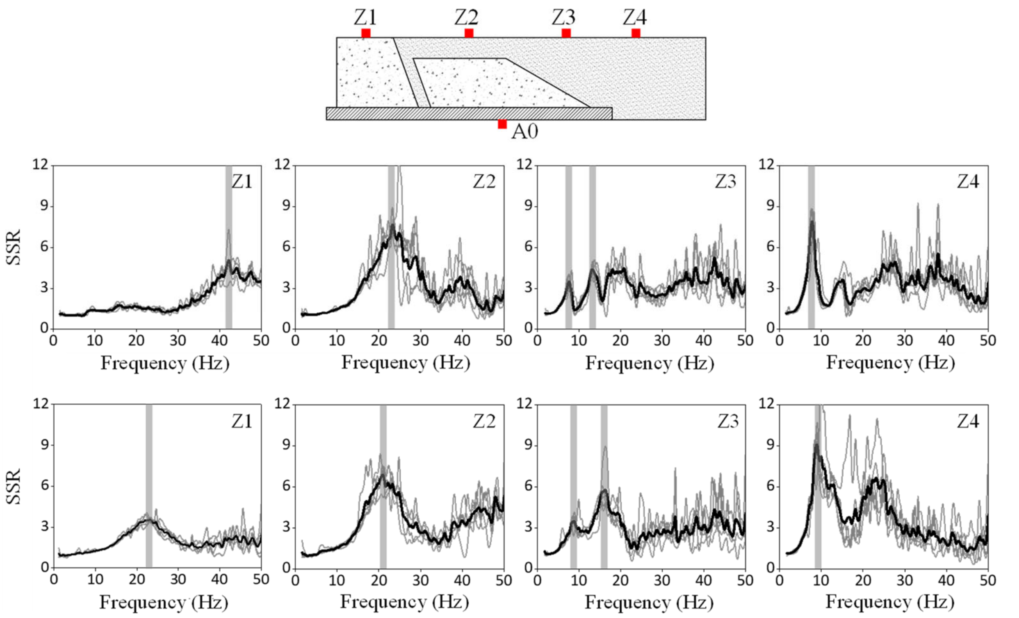

(a)

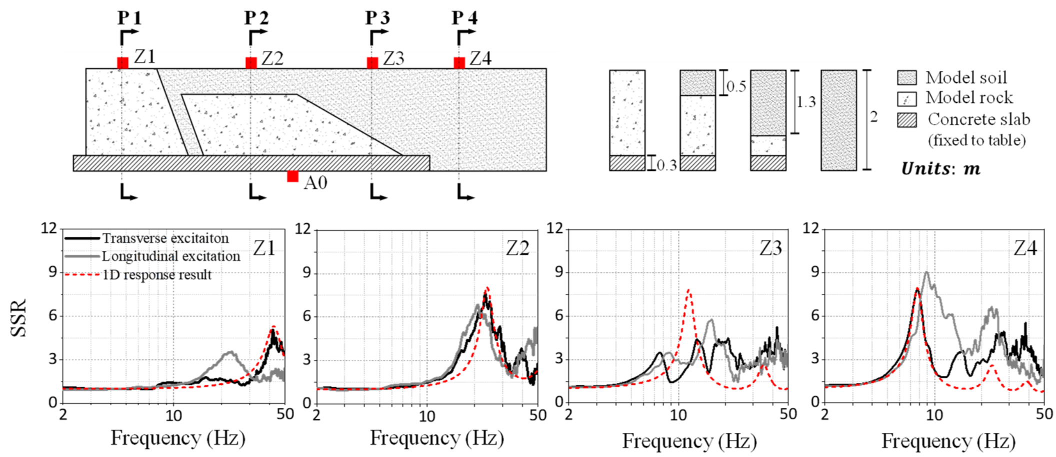

(b)

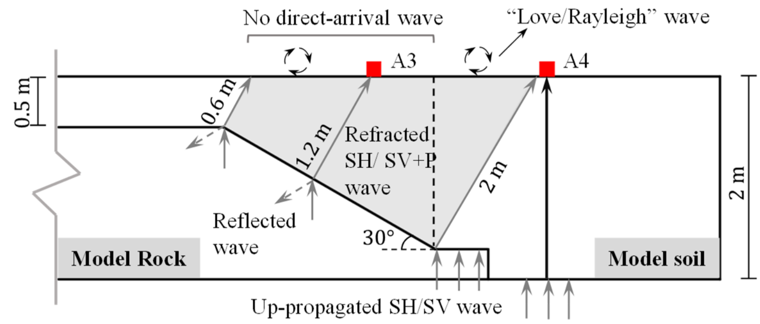

(c)

Figure 11 Local site effect: **(a)** Micro-zones; **(b)** Comparison of SSR results between the experimental and 1D response; and **(c)** Mechanism of wave propagation at the interference.

2.3.1 Local site effect of the soil-rock strata

The standard spectral ratio (SSR) method was used to identify site characteristics. The SSR refers to the spectral ratio of a single record to that of a reference-site record[23]. The first peak of the SSR corresponds to the fundamental frequency, and its amplitude refers to the amplification effect with respect to the reference site. As shown in Fig. 11(a), the site was separated into four micro zones to install the accelerometers, denoted as Z1–Z4, and the signals collected at the shaking table were used as the reference record A0. Fig. 11(a) shows the average SSR results caused by five earthquake sequences excited along both the transverse and longitudinal directions. All results clearly imply a spatial variety of site characteristics caused by the undulation of the underlying bedrock.

To clarify the local site effect caused by variations in strata conditions, the experimental results were compared with the one-dimensional response results, assuming uniform site conditions. The 1D responses can be theoretically calculated using Kramer's method[24]:

$$SSR = \frac{1}{\cos k_1 h_1 \cos k_2 h_2 - \alpha \sin k_1 h_1 \sin k_2 h_2} \tag{3}$$

$$\alpha = \rho_1 V_{\mathrm{d1}} / \rho_2 V_{\mathrm{d2}} \tag{4}$$

$$V_{\mathrm{d}n} = V_{\mathrm{s}n}(1 + i\xi_n); (n = 1,2) \tag{5}$$

$$k_n = 2\pi f / V_{\mathrm{d}n}; (n = 1,2), \tag{6}$$

where V_{s1} and V_{s2} are the shear wave velocities of model soil and model rock, respectively; $i = \sqrt{-1}$; h_1 and h_2 are the thickness of model soil and model rock, respectively; ξ_1 and ξ_2 are the damping ratios of model soil and model rock, respectively; ρ_1 and ρ_2 are the densities of model soil and model rock, respectively; and f is the excitation frequency. The experimental and calculated results are compared in Fig. 11(b). They fit well in the Z2 zone, indicating only a 1D response. Nevertheless, there are two anomalous phenomena when examining the local site effects in Z3 and Z4. One was the double peak observed at Z3 and its complete mismatch with the 1D response. The other is an additional amplification in a specific frequency range at Z4. This can be attributed to the scattered wave generated at the strata interface, which causes an interference effect with the up-propagating waves[25], as illustrated in Fig. 11(c). Local site conditions are likely to cause nonuniform soil–structure interactions when a long tunnel crosses the soil-rock interface.

2.3.2 Dynamic responses of the tunnel in soil-rock strata

Figure 12 shows the spectral acceleration of the three accelerometer pairs as well as their transfer functions (TFs). TF is defined as the tunnel-to-ground spectral ratio. As shown in Fig. 12(c), all the TF values were close to 1, indicating nearly identical movements of the tunnel and surrounding ground. Given that the strata behave differently on either side of the interface, these discrepancies could be transferred to the tunnel. For example, as shown in Figs. 12(a) and (b), when the excitation frequencies were lower than 7 Hz, the soil responded more intensely than the rock. These results were reversed when the excitation frequency was increased to 10 Hz.

These discrepancies may reflect both the sectional deformation and joint extension of the tunnel. The maximum sectional deformations of each section were collected from D1 to D6, and the results are shown in Fig. 13(a). The deformations between D1 and D2 are relatively negligible, but they become significantly larger in the soil deposit, with a maximum of 1.06 mm at D6 in the Sin-7 Hz case. The sharp increase in sectional deformation from the rock stratum to the soil deposit, exemplified by D3 and D4 in Fig. 13(b), is likely to induce significant transverse dislocations between adjacent lining rings near the soil-rock interface. Longitudinally, the segmental tunnel mostly coordinates discrepant movement between soil and rock strata through the joints. Thus, the largest extension of the circumferential joint is expected to occur near the interface, where the relative displacement between the two strata is the most acute. The results aligned with this expectation, as shown in Fig. 13(c). In each excitation case, the largest extension always occurred near the soil–rock interface at J5. When the excitation frequency was 7 Hz, which was close to the fundamental frequency of the model soil, the significant relative displacement between the soil and rock led to an extreme joint extension value.

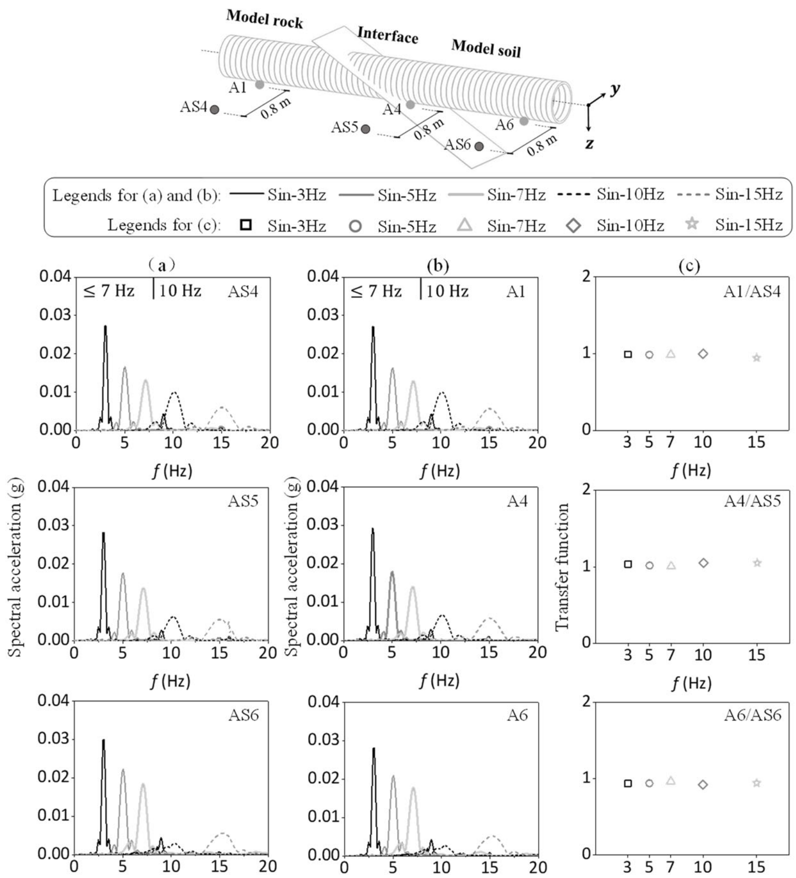

Figure 12 Acceleration responses of the ground-tunnel mode: **(a)** ground; **(b)** tunnel; and **(c)** tunnel-to-ground transfer functions.

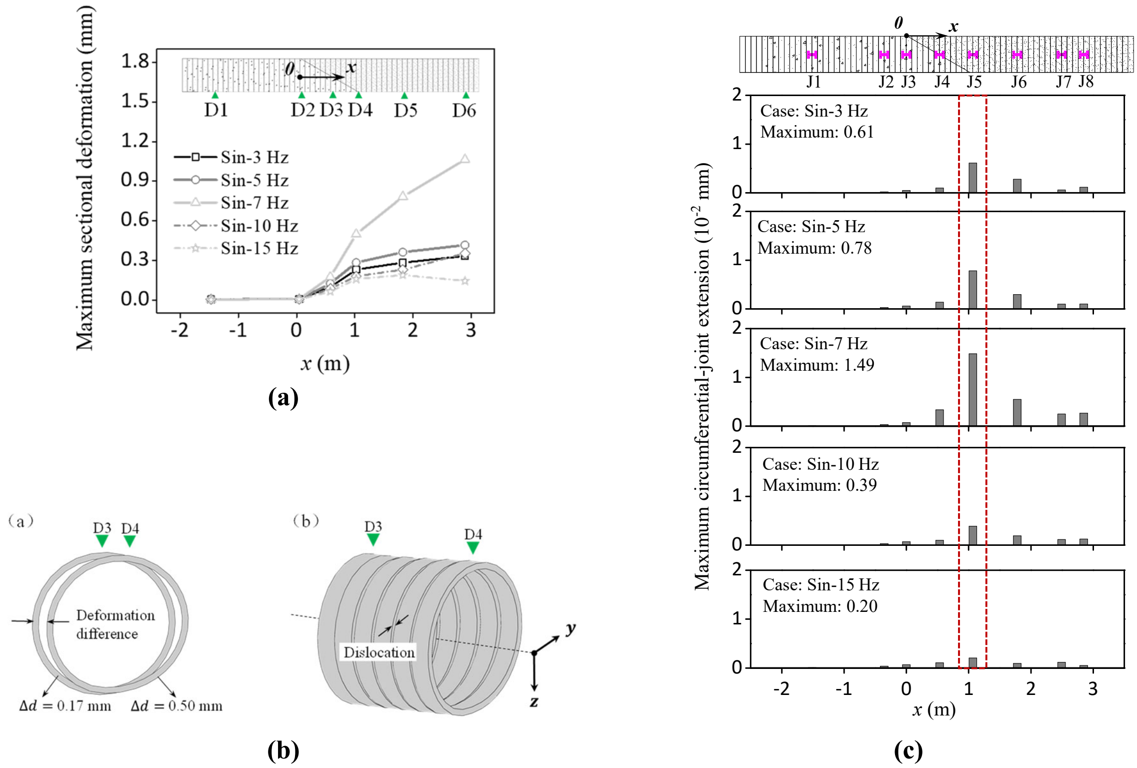

Figure 13 Displacement and deformation: **(a)** Maximum sectional deformations from D1 to D6; **(b)** Deformation difference between D3 and D4; and **(c)** Maximum circumferential-joint extensions.

3. Tunnel in Liquefiable Ground

3.1 *n*-g Tests

A tunnel crossing the ground with liquefiable soil is unavoidable. Case investigations have reported the uplifting or damage of underground structures after earthquakes. To reveal this situation, the mechanism and potential numerical simulation of ground liquefaction have been studied, first in the VELACS project[26] and then in LEAP[27]. Recently Mudahusai at al.[28] investigated the potential uplift of a tunnel with a centrifuge facility. At the elemental level, Seed and Idris[29] provide proof of liquefaction. However, directly applying the results of element tests to a real project remains a challenging task because the physical properties of soils vary with the dimensions of the ground, even if they comprise uniform liquefied saturated soil.

3.2 *1*-g Tests

A temptation to reveal the mechanism of underground structures in liquefiable ground (TUNLIQ) was recently conducted by a joint Sino-German team. One of the tasks was to develop 1-g shaking-table tests for both free-field and site-structure models. To achieve a reasonable goal, a new laminar container was developed[30].

Two tests were conducted on the same liquefiable ground prepared by dry pluviation followed by water saturation. The only difference between the two tests was the loading frequency, as listed in Table 6.

Table 6 Loading cases of shaking table tests: liquefaction of the free-field model.

Test No.	Shaking Event	Frequency (Hz)	PBA (g)	Cycles	Notes
Test 1	T1-E1	2	0.15	20	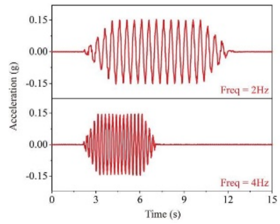
Test 2	T2-E1	4			

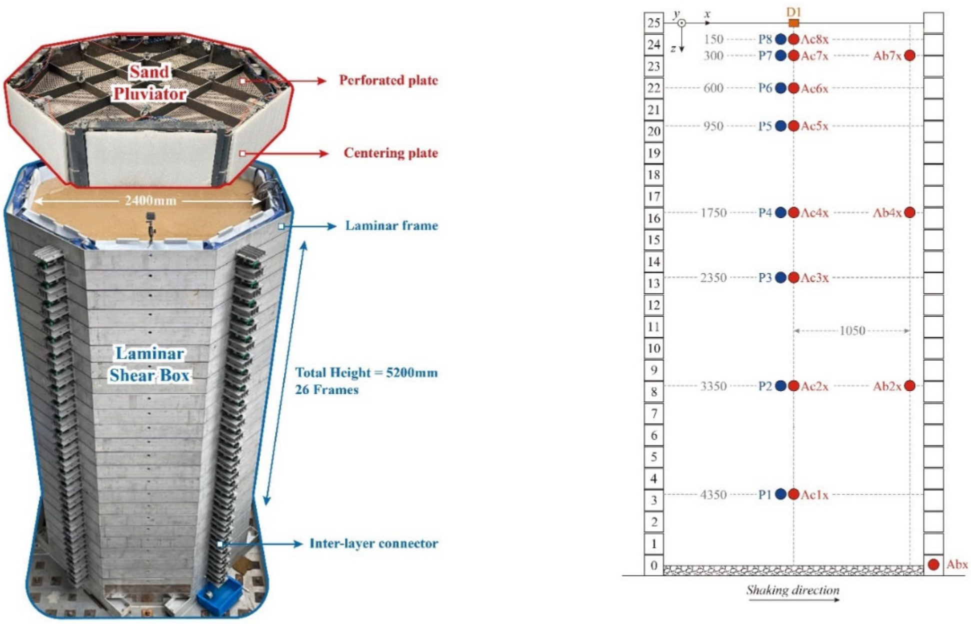

(a) **(b)**

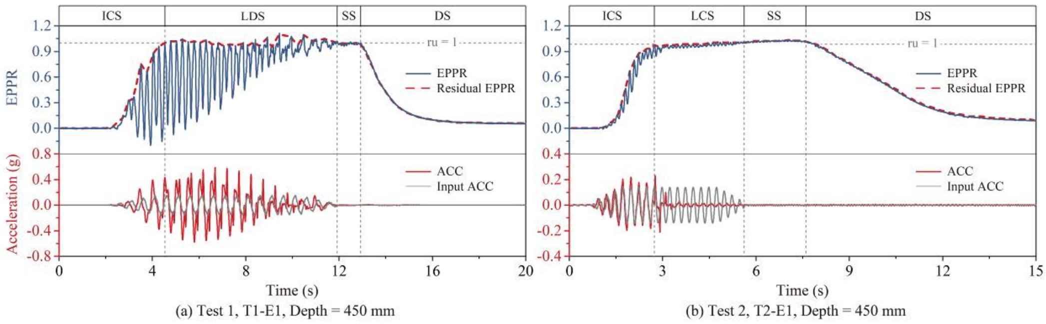

(c)

Figure 14 Liquefication of saturated sand ground: **(a)** Shaking table test for liquefiable ground; **(b)** Instrumentation layout; and **(c)** Time history of EPPR and acceleration at a location 450-mm below ground.

To capture the characteristics of the model ground, sensors including accelerometers and pore pressure gauges were positioned at the target locations, as shown in Fig. 14 (b). The recorded excess pore water pressure (EPWP) can be expressed as the excess pore pressure ratio (EPPR). The time history of the EPPR at the specified observation point can be drawn and matched with the recorded acceleration at the corresponding location and the input acceleration from the table, as shown in Fig. 14(c), for the location 450-mm below the ground. It can be seen that there are distinct behaviors of liquefication between the two tests, although the only difference is the frequency of excitation.

To manifest the phenomenon, liquefaction can be divided into the following stages:

(1) Initial contractive stage (ICS): characterized by predominantly contractive behavior of the soil skeleton and the corresponding accumulation of EPWP in saturated soil. Under cyclic loading, the response of the EPPR exhibits a spiked shape. The positive part of a spike indicates the contraction of the soil skeleton, whereas the negative part implies the dilation of the soil. The transition from the ICS to the subsequent stage occurs once the residual EPPR reaches 1.0. From Fig. 14 (c), the larger oscillation of the EPPR in Test 1 indicates that both the contraction and dilation of the soil under a lower frequency are stronger than that in Test 2, as shown in Fig. 14(c). Correspondingly, the amplitude of the acceleration in Test 1 was more pronounced and lasted for more cycles than that in Test 2.

(2) Liquefied dilative stage (LDS): Under cyclic shearing, the soil experiences alternating contractions and dilations, while the EPPR remains approximately 1.0. At this stage, the soil skeleton loses and regains its shear stiffness throughout the repeated contractive-dilative cycles, which facilitates the development of large strains. This type of liquefaction is referred to as 'cyclic mobility' liquefaction. It should be noted that the LDS was developed only in Test 1.

(3) Liquefied contractive stage (LCS): represents contraction-dominated soil behavior with minimal dilation spikes during continuous cyclic loading. When the effective stress was maintained at zero, the soil loses its strength completely and becomes flowable. Thus, the liquefaction that occurred in LCS is defined as 'cyclic instability,' which is only observed in Test 2.

(4) Seepage stage (SS): the stage when the EPPR maintains at 1.0 after the LDS or LCS although there is no input of excitation. This stage was encountered only in shallow areas and can be attributed to the continuous supply of pore water by the upward seepage of pore water from deeper zones. The SS period in Test 2 was longer than that in Test 1.

(5) Dissipation stage (DS): primarily characterized by the dissipation of the EPWP. Clearly, the DS of Test 1 was significantly shorter than that of Test 1.

It can be concluded from the above discussion that 'cyclic instability' of ground will result from high-frequency excitation but 'cyclic mobility' from low-frequency excitation.

3.2.1 Free-field liquefaction under multiple shakings

Previous field observations and model tests have shown that the resistance of a field to liquefaction can vary significantly under multiple shaking events. To investigate the effect of frequency on the liquefaction behavior of soil deposits during consecutive earthquakes, two parallel 1-g shaking table tests were conducted. Identical soil models comprising Fujian medium sand were prepared in the biLSB using a sand pluviator, as shown in Fig. 14 (a), where four identical excitations were applied sequentially after the excess pore pressure from the previous events had fully dissipated. The only difference between the two tests was the loading frequency.

To facilitate a comparison of liquefaction resistance between liquefied and non-liquefied areas, two factors were analyzed: the liquefaction resistance was defined by N_L , representing the number of loading cycles required to trigger the initial liquefaction. In non-liquefied areas, the resistance is indicated by the maximum excess pore pressure $r_{\mathrm{u,max}}$. Fig. 15 shows a comparison of the liquefaction resistance across each shaking event.

In the first shaking event, a comparison of N_L revealed that fewer loading cycles were required to trigger liquefaction at lower loading frequencies. However, a higher loading frequency induced liquefaction across significantly deeper zones. These differences were attributed to the compound effects of the loading frequency, which influenced both the local loading amplitudes and relative drainage conditions. Despite variations in soil behavior, the evolution of liquefaction resistance across multiple shaking cycles was consistent in both tests: the resistance to reliquefaction in the liquefied area significantly decreased during the second shaking event and began to recover from the third event onward, whereas the resistance in the unliquefied area increased monotonically with each event.

In conclusion, it is crucial to consider the frequency effect of the input motion on the dynamic response of a soil deposit during earthquakes. For liquefiable soil layers, which often coincide with the depths of the underground transportation infrastructure, aftershocks may cause more severe damage because the field resistance to liquefaction can be further reduced even after the initial liquefaction has occurred.

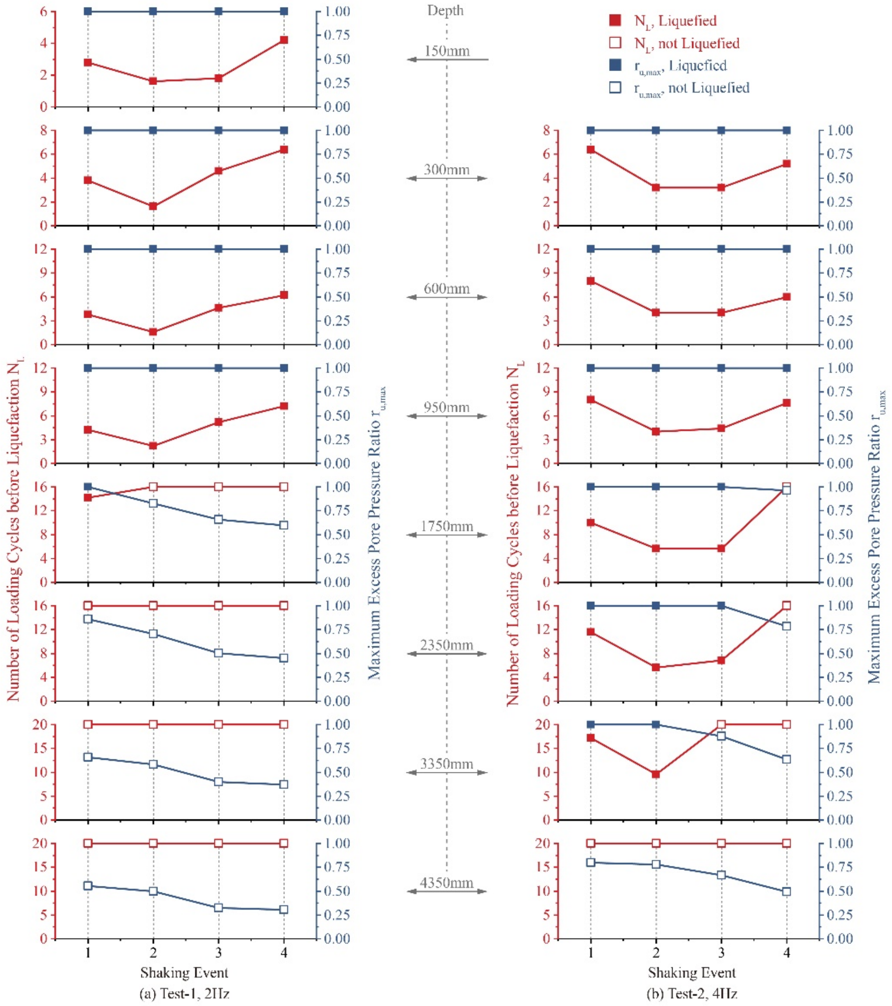

Figure 15 Liquefaction under multiple shakings: **(a)** Test-1, 2 Hz; and **(b)** Test-2, 4 Hz.

3.2.2 Distinct tunnel uplifting behavior during liquefaction under multiple shakings

During soil liquefaction, the interaction between soil and structure (SSI) is influenced not only by the macroscopic parameters of the structure, but also by the microscopic characteristics of the soil-structure interface. To examine how the structural surface roughness affects the SSI during ground liquefaction, a site tunnel 1-g shaking table test was conducted. As depicted in Fig. 16(a), the model tunnel was segmented into two sections: the left side was covered with sandpaper to create a nonslip interface, while the right side was coated with Teflon tape to simulate a nearly frictionless interface. The tunnel had an overall density of 900 kg/m^3 and was embedded 300-mm deep in a soil model with a relative density of 50%. The site-tunnel model was subjected to two seismic motions, each with a frequency of 4 Hz but differing in amplitude, as listed in Table 7.

Table 7 Loading cases of shaking table tests: liquefaction of the site-tunnel model.

Case	Frequency	Peak Base Acceleration	Number of cycles
ST-E1	4	0.15g	20
ST-E2	4	0.30g	20

The pore pressure responses for the two shaking events are compared in Fig. 16 (b). This shows that in ST-E1, only a part of the field underwent liquefaction owing to the limited loading amplitude. In contrast, the liquefaction affected the entire ST-E2 field. Figures 16(c) and 16(d) compare the vertical displacements of the tunnel and ground surface, revealing that the uplift behavior of the tunnel varies with the surface roughness. In ST-E1 (Fig. 16 (c)); despite partial liquefaction, the tunnel experienced significant uplift. This uplift occurred in two stages: Stage 1, where the uplift was rapid and steady during the seismic input; and Stage 2, where the uplift slowed as the excess pore pressure (EPP) dissipated and the soil consolidated. The smooth segment of the tunnel exhibited slightly more uplift than the rough segment. In ST-E2 (Fig. 16(d)), the increased loading amplitude led to significant variations in the uplift behavior. Four distinct stages of vertical displacement were identified. In Stage 1, the tunnel initially settled as excess pore pressures accumulated. During Stage 2, both tunnel segments experienced uplift at similar rates owing to full liquefaction. The most pronounced difference in uplift rate between the segments occurred in Stage 3, where the smooth segment uplifted 2.3 times faster than the rough segment as EPPs decreased. This disparity is attributed to the increased frictional resistance resulting from the recovery of the effective normal stress owing to pore pressure dissipation during this stage. Finally, in Stage 4, the tunnel settles as the resistance exceeds the upward forces.

In summary, the tunnel uplift behavior varied with the structural surface roughness and amplitude of the input motions. Surface roughness has a pronounced effect on tunnel uplift, particularly during reconsolidation after liquefaction.

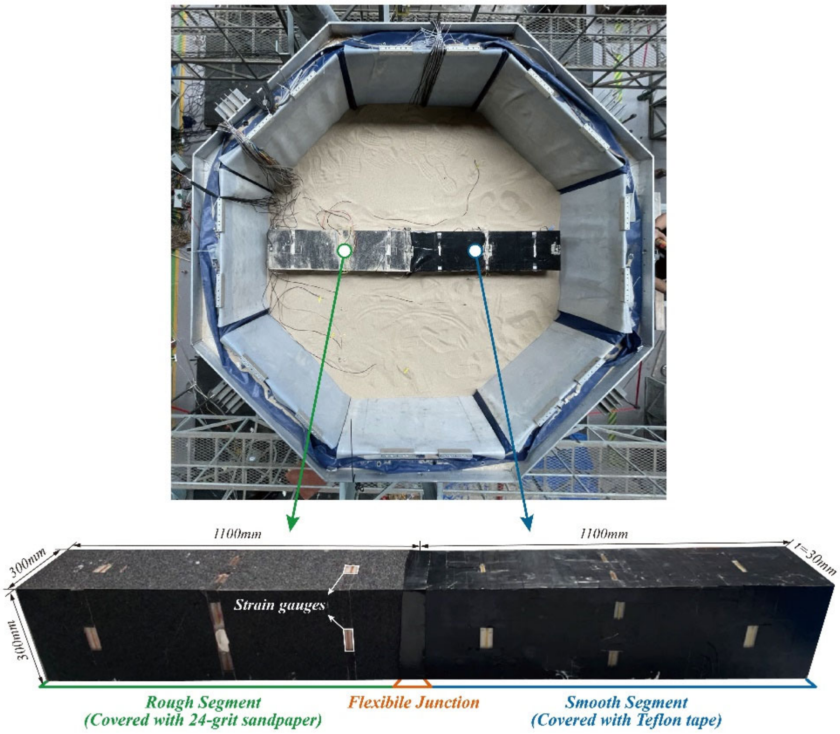

(a)

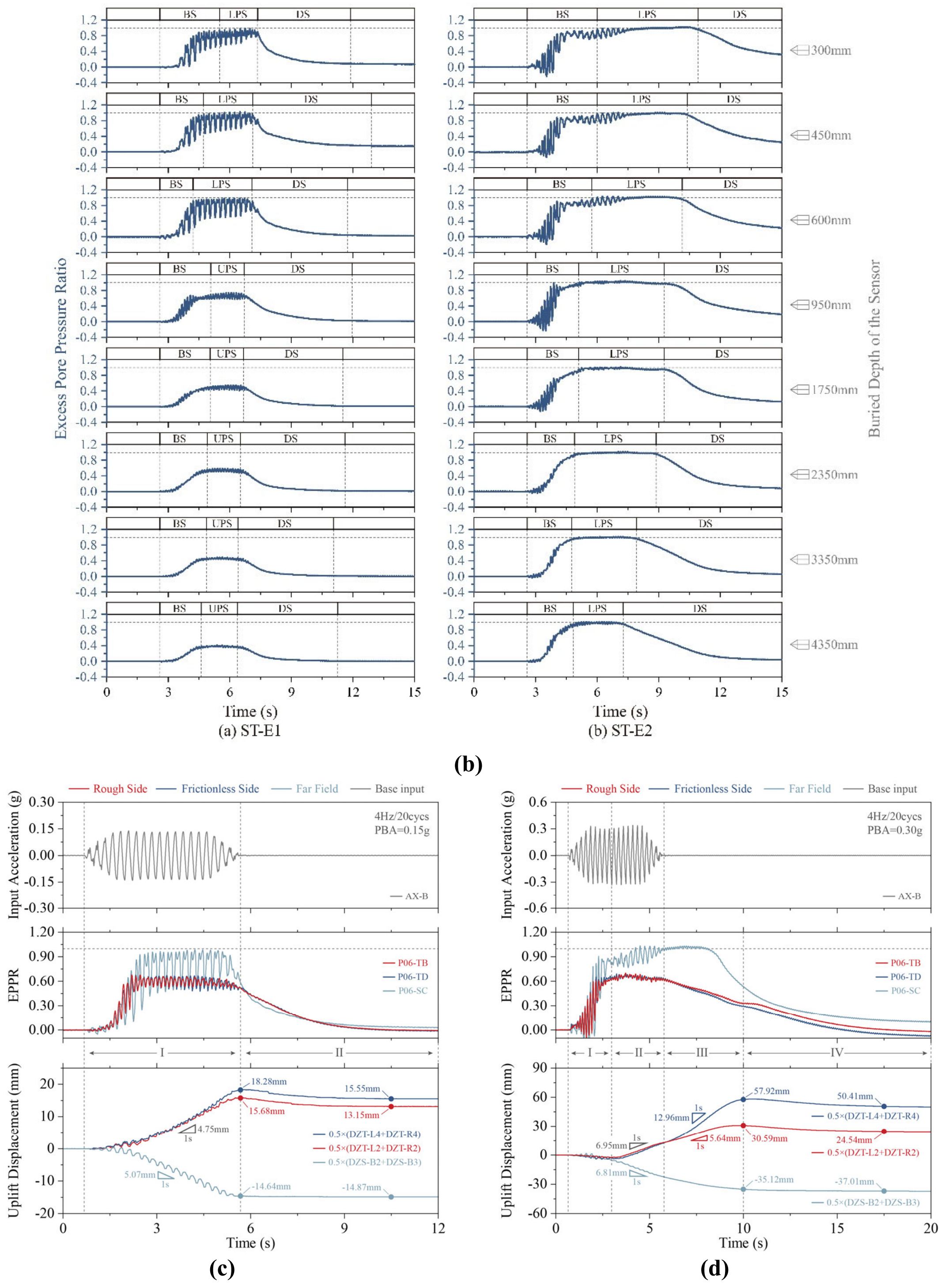

Figure 16 Distinct tunnel uplifting behavior during liquefaction under multiple shakings: **(a)** Model tunnel; **(b)** Pore pressure responses in shaking events ST-E1 and ST-E2; **(c)** Uplifting behavior in ST-E1; and (d) Uplifting behavior in ST-E2.

4. Tunnel crossing Fault

Seismological studies have indicated that the zones in which tunnels cross faults are particularly vulnerable to seismic damage. Over the past 30 years, a considerable number of fault-crossing tunnels have experienced damage during earthquakes, including the 1999 Chi-Chi earthquake[31], 2004 Niigata earthquake[32], 2008 Wenchuan earthquake[33], 2016 Kumamoto earthquake[34], 2022 Menyuan earthquake[35], and 2023 Turkey earthquake[36]. During these seismic events, most fault-crossing tunnels suffered severe damage, such as lining collapse, primarily owing to the impact of fault movement.

Extensive research has been conducted on the failure mechanisms of tunnels crossing active faults and subjected to fault ruptures[37–39]. However, even if faults do not rupture during earthquakes, tunnels may sustain damage. Several studies have addressed this issue[40–42]. Evidence indicates that essential differences exist between these two conditions. Tunnels crossing ruptured faults are primarily damaged by violent fault dislocations, whereas tunnels crossing faults without ruptures may experience differential movements induced by the fault site effect.

To this end, a large-scale physical model was developed to consider a scenario in which a model tunnel crosses an unruptured fault under seismic vibrations, as shown in Fig. 17, along with the layout of the instrumentation. The local site effect of the fault site[43], as well as the deformation pattern and failure mechanism of the fault-crossing tunnel[44,45], were investigated using this shaking table test.

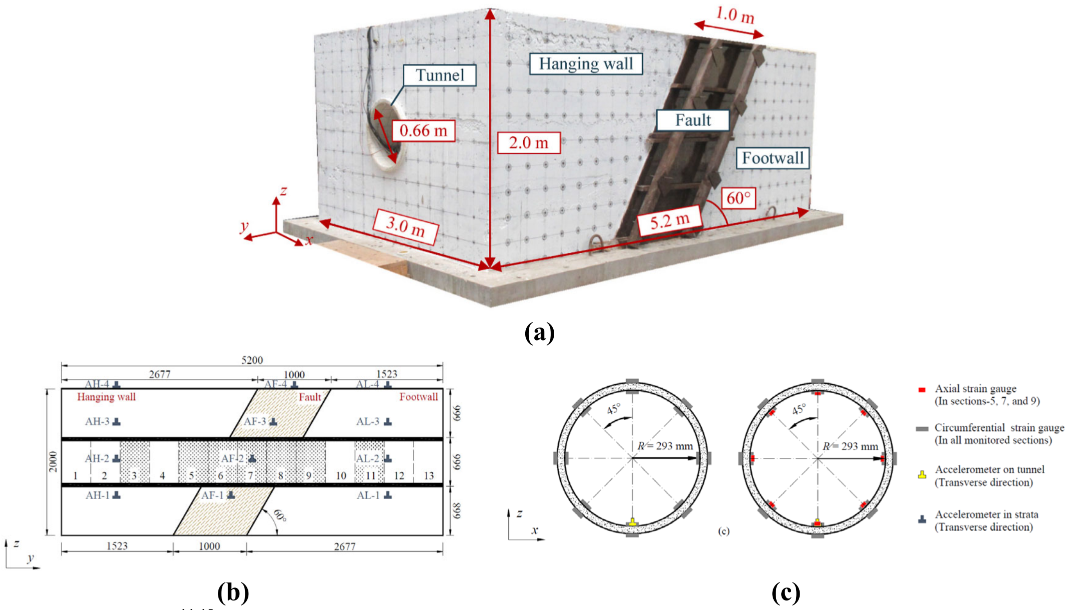

Figure 17 Testing model[44,45]: **(a)** Physical model; **(b)** Instrumentations (longitudinal profile); and **(c)** Instrumentations (cross-sectional profile of tunnel).

4.1 Fault site effect and acceleration response of tunnel

Figure 18 (a) plots the TFs of the fault site in the tests against the analytical solution of the one-dimensional site. The hanging wall and the footwall, although homogeneous in the vertical direction, have significant discrepancies from the one-dimensional site responses. The fault exhibits some similarities with the one-dimensional site response under transverse excitation, but with a more pronounced amplification effect. Under longitudinal excitation, the fault exhibits completely different response from the one-dimensional site response. The accelerograms of the ground surface of the fault site in sinusoidal wave cases are shown in Fig. 18(b). A significant alteration of the accelerogram waveform relative to the input seismic motion could be found, attributed to frequency dispersion and waveform conversion, as shown in Fig. 18(c). The generation of components at 30 Hz and 45 Hz, which were not observed in the original signal, indicates the presence of harmonic distortion. This provides strong evidence of the non-linearity of the strata within the fault.

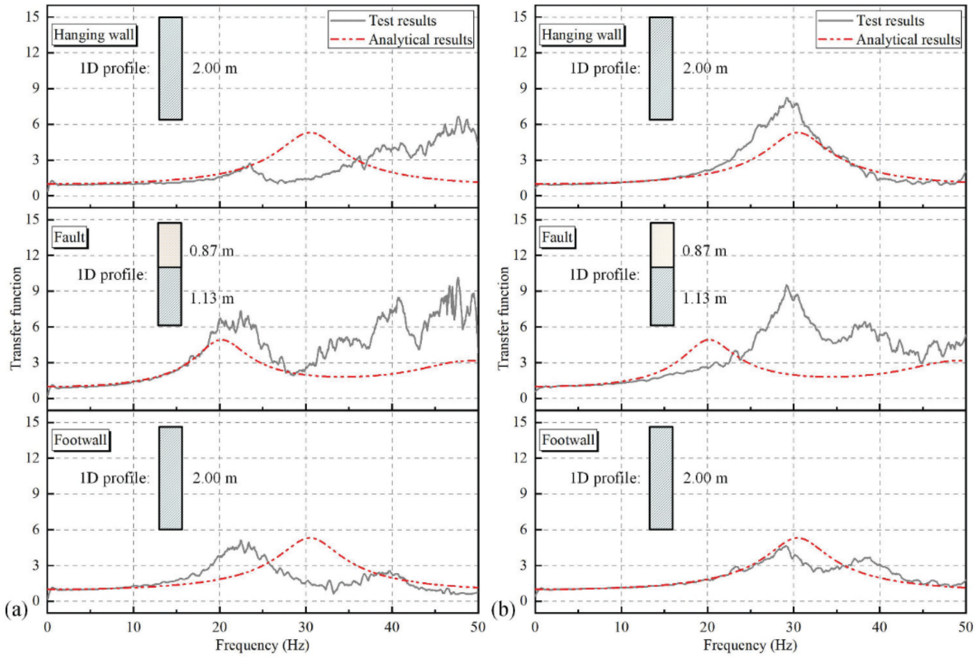

Transverse excitation

Longitudinal excitation

(a)

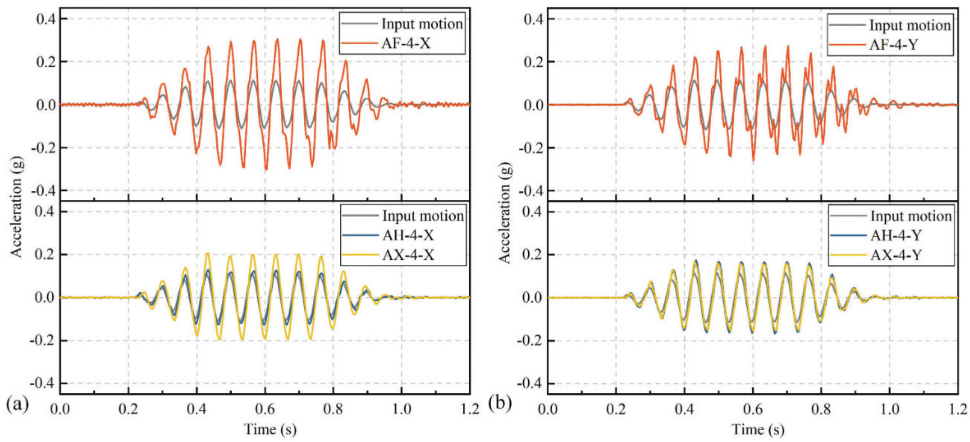

Transverse excitation

Longitudinal excitation

(b)

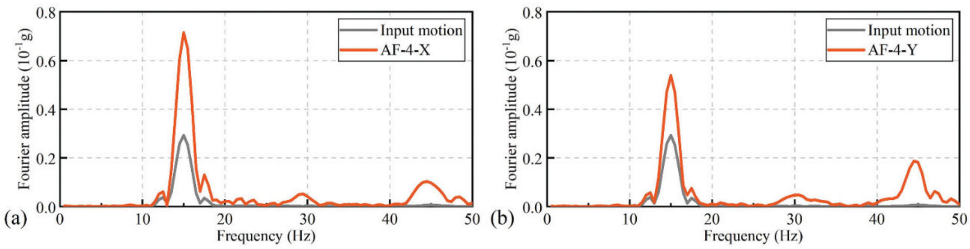

Transverse excitation

Longitudinal excitation

(c)

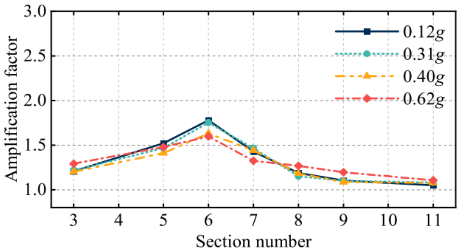

(d)

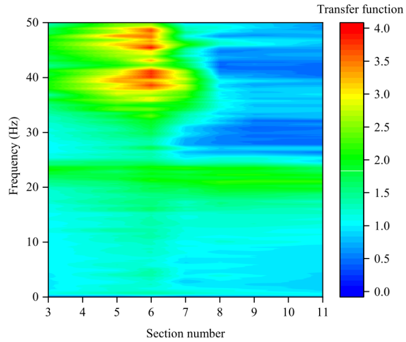

(e)

Figure 18 Micro-zonation of site effect[43]: **(a)** Comparison between transfer functions of strata and 1D analytical results: transverse and longitudinal excitation; **(b)** Accelerograms of strata in sinusoidal wave cases: transverse and longitudinal excitation; **(c)** Fourier spectra of strata within fault in sinusoidal wave cases: transverse and longitudinal excitation; **(d)** Acceleration amplification factors of the tunnel; and **(e)** Transfer functions of the tunnel.

Figure 18(d) shows the acceleration amplification factors of the tunnel. In all the test cases, the curves peaked near the fault. The strongest accelerations of the tunnel were always registered in section-6, which intersects the interface of the fault and hanging wall. Figure 18(e) shows the contours of the transfer functions of the tunnel sections in the white noise case. Generally, sections of the tunnel in the hanging wall exhibited higher amplifications than those in the footwall, and the responses in section-6 were the most amplified.

4.2 Deformation pattern and failure mechanism

The maximum radial deformation of the tunnel is shown in Fig. 19(a). The tunnel exhibits shearing deformation under transverse excitation and vertical crush deformation under longitudinal excitation. Figure 19(b) shows the maximum strain in the tunnel. The largest strains were found in section-6, followed by sections-5 and 7, and the strains of the tunnel sections in the hanging wall exceeded those in the footwall.

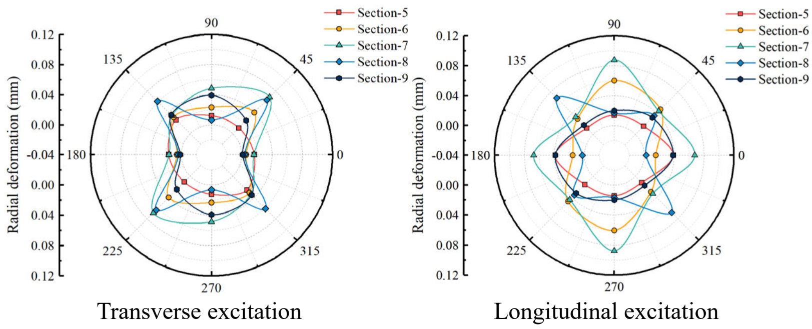

(a)

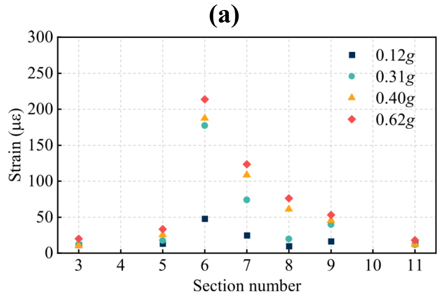

(b)

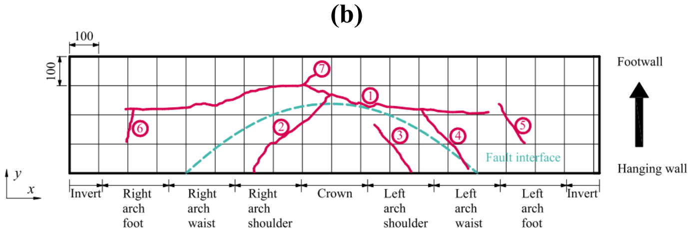

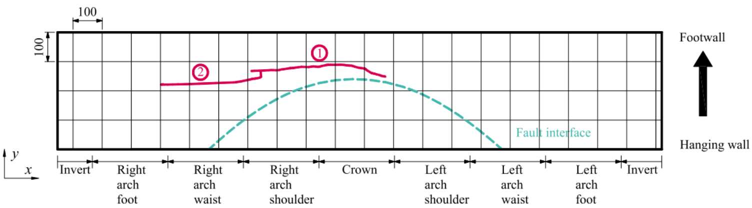

(c)

Figure 19 Deformation and failure pattern[45]: **(a)** Maximum radial deformation of the tunnel: transverse and longitudinal excitation; **(b)** Maximum strain of the tunnel; and **(c)** Lining cracks of the tunnel.

The structural integrity of the tunnel was assessed meticulously at the end of each test. It can be expected that section-6, which had the strongest accelerations and the largest strains, also had the most cracks. As shown in Fig. 19(c), the lining exhibited seven cracks. The primary crack aligned with the fault interface and extended to approximately 1300 mm in length. On both the interior and exterior, cracks mostly initiated from the crown and developed towards the invert while maintaining an orientation roughly parallel to the fault interface.

4.3 Analytical model

A pseudo-static analytical model was established based on the shaking table test data to further explore the deformation pattern and failure mechanism of the tunnel. The fault-rock-tunnel system was simplified as a Timoshenko beam on Winkler foundations, as shown in Fig. 20(a). At a certain moment *t*, the governing equation for a Timoshenko beam on a Winkler foundation is

$$\frac{\partial^4 u_\mathrm{t}}{\partial x^4} - \frac{K_\mathrm{h}}{K_\mathrm{t}}\frac{\partial^2 u_\mathrm{t}}{\partial x^2} + \frac{K_\mathrm{h}}{E_\mathrm{t} I_\mathrm{t}} u_\mathrm{t} = -\frac{K_\mathrm{h}}{K_\mathrm{t}}\frac{\partial^2 u_\mathrm{g}}{\partial x^2} + \frac{K_\mathrm{h}}{E_\mathrm{t} I_\mathrm{t}} u_\mathrm{g}, \tag{7}$$

where E_t is the elastic modulus of the tunnel; I_t is the moment of inertia of the tunnel cross-section; u_t is the horizontal transverse displacement of the tunnel; u_g is the horizontal displacement of the ground at the depth of the tunnel; K_h is the spring stiffness of the Winkler foundations, and K_t is the transverse shear stiffness of the Timoshenko beam calculated as follows:

$$\begin{cases} K_\mathrm{h} = \dfrac{16\pi G_\mathrm{g}(1-\nu_\mathrm{g})D}{4H(3-4\nu_\mathrm{g})} \\ K_\mathrm{t} = G_\mathrm{t} A_\mathrm{t} \dfrac{2(1+\nu_\mathrm{t})}{4+3\nu_\mathrm{t}} \end{cases} \tag{8}$$

The boundary and continuity conditions of the tunnel are:

$$\begin{cases} \lim\limits_{x\to-\infty} u_\mathrm{t} = u_{\mathrm{g}1} \\ \lim\limits_{x\to+\infty} u_\mathrm{t} = u_{\mathrm{g}2} \\ \lim\limits_{x\to0^-} u_\mathrm{t} = \lim\limits_{x\to0^+} u_\mathrm{t},\ \lim\limits_{x\to L^-} u_\mathrm{t} = \lim\limits_{x\to L^+} u_\mathrm{t} \\ \lim\limits_{x\to0^-} \theta = \lim\limits_{x\to0^+} \theta,\ \lim\limits_{x\to L^-} \theta = \lim\limits_{x\to L^+} \theta \\ \lim\limits_{x\to0^-} M = \lim\limits_{x\to0^+} M,\ \lim\limits_{x\to L^-} M = \lim\limits_{x\to L^+} M \\ \lim\limits_{x\to0^-} Q = \lim\limits_{x\to0^+} Q,\ \lim\limits_{x\to L^-} Q = \lim\limits_{x\to L^+} Q \end{cases} \tag{9}$$

The deflection angle θ, the bending moment M, and the shear force Q can be easily derived from the following equations:

$$\begin{cases} M = -E_\mathrm{t} I_\mathrm{t}\left(\dfrac{\partial^2 u_\mathrm{t}}{\partial x^2} - \dfrac{\partial \beta}{\partial x}\right) \\ Q = K_\mathrm{t}\beta \\ \theta = \dfrac{\partial u_\mathrm{t}}{\partial x} - \beta \end{cases} \tag{10}$$

The displacement of the fault-crossing tunnel can be obtained by incorporating a general solution with boundary and continuity conditions. The shear forces in the tunnel derived from the analytical solution are shown in Fig. 20(b). Neither was symmetrical about the fault. In particular, the shear force increased sharply at the interface between the fault and the hanging wall. This explains the localized damage to the tunnel in the area. The longitudinal non-uniform deformations of the fault site are the primary cause of the shearing of the tunnel, as illustrated in Fig. 20(c). The difference between the tunnel cross-sections is fundamentally the relative horizontal displacement at two different heights of the cross-section. The differential tensions/compressions and rotations inevitably result in shear–torsional deformation of the tunnel, as illustrated in Fig. 20(c). This deformation pattern was the most prominent at the crown of the tunnel and corresponded to the concentration of cracks at the crown.

Although a series of studies have been conducted on the seismic response of tunnels crossing non-ruptured faults, several critical issues remain unresolved. First, the failure mechanisms of tunnels under the coupled effects of intense seismic vibrations and fault ruptures, as well as the corresponding mitigation strategies, require further investigation. When an active fault ruptures, the dynamic interaction between the fault dislocation and the stress waves generated by the rupture creates a coupling effect. Simply considering either fault dislocation or seismic vibration is insufficient for accurately revealing the failure mechanisms of tunnels. Second, the impact of cascading fault ruptures on the seismic response of tunnels presents a significant challenge. Compared with a single fault, the seismic mechanism of cascading fault ruptures is more complex. The failure mechanisms of tunnels under such scenarios represent a current scientific frontier issue. Finally, the development of analytical methods to determine the seismic response of tunnel-crossing faults remains challenging. The complexity of the wave field at the fault site during earthquakes, combined with the highly nonlinear mechanical behavior of fractured rock masses within the fault, makes it difficult to determine the free-field response of the fault site. This poses severe challenges for the analytical methods for tunnel-crossing faults.

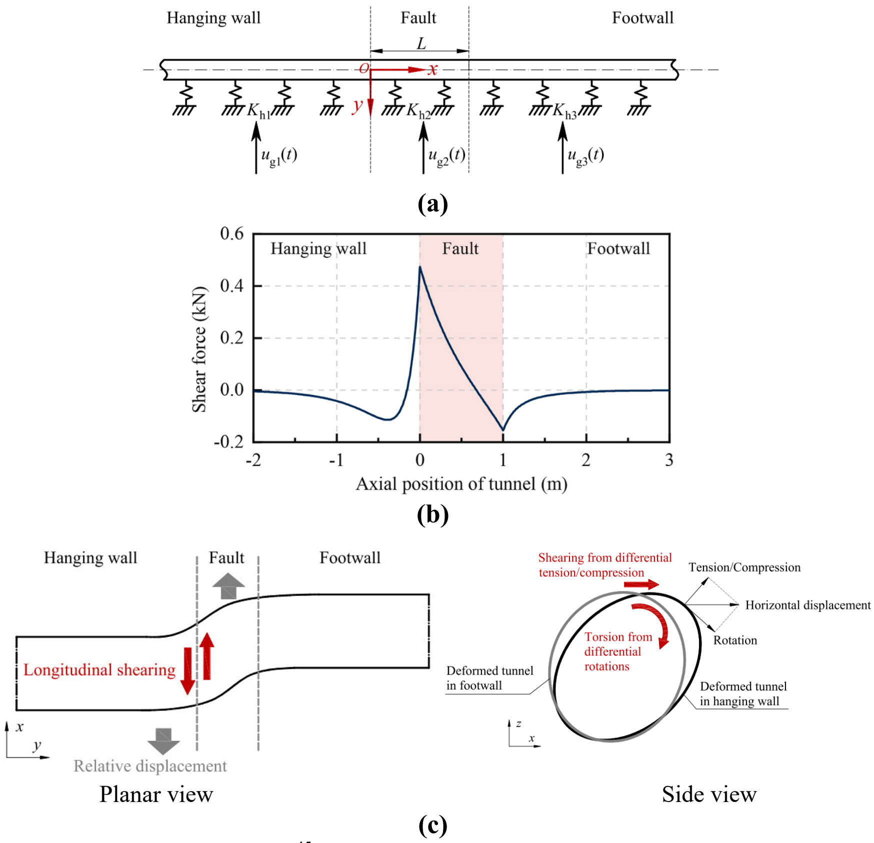

Figure 20 Analytical model of fault-crossing tunnel[45]: **(a)** Analytical model; **(b)** Shear forces of the tunnel; and **(c)** Longitudinal and transverse deformation patterns of fault-crossing tunnel.

5. Closing Remarks

A series of large-scale shaking table tests were conducted on scenarios of long tunnels, such as under travelling waves, conjunction structures between the shaft and tunnel, variation of rock-soil ground, uplift in liquefiable ground, and crossing faults. The results were examined in contrast to numerical or analytical solutions and the following conclusions were drawn.

5.1 Travelling wave

The propagation of travelling waves exhibit spatial variation in any domain of the ground, which is indicated by the spectrum representing the impact of wave superposition, whether on uniform ground or sloped ground. Comparing the uniform excitation and the same intensity of non-uniform excitation, no significant difference in the magnitude of acceleration was observed at a measuring spot. The differential displacement of the tunnel under non-uniform excitation is propagated from one end to the other in times of that of the uniform excitation. The joint dislocations thus propagated. Non-uniform excitation from earthquakes should be considered in the aseismic design of long tunnels.

5.2 Structural variation

Discrepant responses due to structural variations were directly revealed by the test, and the data were interpreted using the classic pseudo-static model. Based on this, a dynamic analytical model for the shaft-tunnel junction was developed by combining the beam-spring model and the dynamic model for rigid caissons. The dynamic model was validated using 3-dimensional numerical computations. Its applicability was further extended to incorporate the travelling-wave effect, where the spatial displacement field was calculated using the stiffness matrix method for layered media. The newly proposed method yielded satisfactory results for the displacements of the shaft and internal forces of the tunnel. It also quantitatively clarifies the soil-structure interaction mechanism of the tunnel-shaft junction.

5.3 Variation of ground

The site characteristics of strata with longitudinally varying geological conditions exhibited spatial variations that were identified using the standard spectral ratio (SSR) method. These spatial variations were specified by comparison with 1D theoretical analysis results. The amplification effect observed in soft ground can be explained by the interference effect resulting from the scattered waves generated at the strata interface. The tunnel portions follow the nonuniform movements of the varying strata, thereby reflecting the resulting discrepant responses, as revealed by the acceleration data. The tunnel deformation was negligible in the rock stratum, whereas it was significantly greater in the soil deposit. Notably, the sharp increase in the sectional deformation when transitioning from the rock stratum to the soil deposit is likely to induce significant transverse dislocations between adjacent lining rings. Circumferential joint extensions were concentrated near the strata interface and their magnitudes were determined by the relative displacement between the two strata. Based on the test data, the influence of the stratum interface was primarily limited to the region within three times the tunnel diameter.

5.4 Liquefiable ground

Liquefaction is associated with the accumulation of pore water pressure owing to the volumetric contraction of soils under undrained cyclic loading conditions. For cohesionless soils, the development of excess pore water pressure induces a loss of grain contact, which ultimately leads to the disappearance of shear stiffness. The results from the 1-g shaking table tests show that the dynamic behavior of the soil is significantly influenced by the frequencies of the input seismic motions. This variation can be attributed to the combined effects of the localized strain amplitude and relative drainage conditions. Owing to the viscous movement of liquefied soils and the dynamic migration of pore fluids, underground structures often exhibit uplift behavior during liquefaction. The experimental findings also revealed that the surface roughness of the structure played a critical role in the tunnel uplift, with smoother surfaces experiencing significantly greater uplift during liquefaction.

5.5 Crossing fault

The fault exhibits a higher acceleration response than the strata on both its sides. A significant alteration in the accelerogram waveform relative to the input seismic motion was observed on the surface of the fault, which could be attributed to frequency dispersion and waveform conversion. The maximum acceleration of the tunnel was located at the interface between the fault and hanging wall, whereas the maximum strain of the tunnel also appeared in this area. After seismic excitation, several cracks parallel to the fault interface were observed on both the interior and exterior of the tunnel and were mainly distributed near the interface between the fault and hanging wall. An analytical model was established to further investigate the deformation patterns and failure mechanisms of the tunnel. The sharply increased shear force at the interface between the fault and hanging wall, which was derived from the analytical solution, explains the localized damage to the tunnel in the area. The differential tensions/compressions and rotations inevitably result in shear–torsional deformation of the tunnel, which is the primary culprit behind the shearing of the tunnel.

Although these investigations clarified the most critical situations of long tunnels under seismic action, there are still some cases to be explored. One of the unveiled scenarios is a tunnel crossing a potential rupture fault. Other aspects include measures for improving the resilience of tunnels in mitigating seismic hazards. This is one method of achieving sustainable development.

Acknowledgement

The authors express their gratitude to the team for their assistance in preparing this manuscript. Financial support from the NSFC (52061135112) and others is also acknowledged.

References

1. John CMS, Zahrah TF. Aseismic Design of Underground Structures. Tunnelling and Underground Space Technology. 1987;2(2):165-197.
2. Wang JN. Seismic Design of Tunnels: A Simple State-of-the-Art Design Approach. Parsons Brinckerhoff; 1993.
3. Hashash YMA, Hook JJ, Schmidt B, I-Chiang Yao J. Seismic design and analysis of underground structures. Tunnelling and Underground Space Technology. 2001;16(4):247-293.
4. Tsinidis G, de Silva F, Anastasopoulos I, et al. Seismic behaviour of tunnels: From experiments to analysis. Tunnelling and Underground Space Technology. 2020;99:103334.
5. Ministry of Housing and Urban-Rural Development. Standard for Seismic Design of Underground Structures. China Construction Press; 2018.
6. Newmark NM. Problem in wave propagation in soil and rock. In: Proceedings of Int. Symp. Wave Propagation and Dynamic Properties of Earth Materials. Univ. New Mexico Press; 1968:7-26.
7. Kuesel TR. Earthquake Design Criteria for Subways. Journal of the Structural Division. 1969;95(6):1213-1231.
8. Yu H, Yuan Y. Analytical solution for an infinite Euler-Bernoulli beam on a viscoelastic foundation subjected to arbitrary dynamic loads. Journal of Engineering Mechanics. 2014;140(3):542-551.
9. Yuan Y, Yu H, Li C, Yan X, Yuan J. Multi-point shaking table test for long tunnels subjected to non-uniform seismic loadings – Part I: Theory and validation. Soil Dynamics and Earthquake Engineering. 2018;108:177-186.
10. Yu H, Yuan Y, Xu G, Su Q, Yan X, Li C. Multi-point shaking table test for long tunnels subjected to non-uniform seismic loadings-part II: Application to the HZM immersed tunnel. Soil Dynamics and Earthquake Engineering. 2018;108:187-195.
11. Bao Z, Yuan Y, Yu H. Multi-scale physical model of shield tunnels applied in shaking table test. Soil dynamics and earthquake engineering. 2017;100:465-479.
12. Zhang J, Yuan Y, Yu H. Shaking table tests on discrepant responses of shaft-tunnel junction in soft soil under transverse excitations. Soil Dynamics and Earthquake Engineering. 2019;120:345-359.
13. Zhang J, Yuan Y, Bao Z, Yu H, Bilotta E. Shaking table tests on the intersection of cross passage and twin tunnels. Soil Dynamics and Earthquake Engineering. 2019;124:136-150.
14. Zhang J, Yuan Y, Bao Z, Yu H, Bilotta E. Shaking table tests on shaft-tunnel junction under longitudinal excitations. Soil Dynamics and Earthquake Engineering. 2020;132:106055.
15. Zhang J, Yuan Y, Bilotta E, Zhang B, Yu H. Analytical solution for dynamic responses of the vertical shaft in a shaft-tunnel junction under transverse loads. Soil Dynamics and Earthquake Engineering. 2019;126:105779.
16. Zhang J, Yuan Y, Zhang B, Bilotta E. Analytical solutions for seismic responses of the tunnel in a shaft-tunnel junction under transverse excitations. Soil Dynamics and Earthquake Engineering. 2019;127:105826.
17. Zhang J, Yuan Y, Bilotta E. Analytical solutions for seismic responses of shaft-tunnel junction under longitudinal excitations. Soil Dynamics and Earthquake Engineering. 2020;131:106033.
18. Zhang J, Yuan Y, Xiao M, Yin Y, Sun Q. Closed-form solution for dynamic responses of shaft-tunnel junction under uniform P waves. Underground Space. 2022;7(3):352-362.
19. Gazetas G. Formulas and charts for impedances of surface and embedded foundations. Journal of geotechnical engineering. 1991;117(9):1363-1381.
20. Zhang J, Xiao M, Bilotta E, Li C, Yuan Y. Analytical solutions for seismic responses of shaft-tunnel junction under travelling SH-wave. Tunnelling and Underground Space Technology. 2021;112:103910.
21. Zhang J, Yuan Y, Sun Q. Dynamic analytical model for shaft-tunnel junction under P-SV waves. Applied Mathematical Modelling. 2022;112:91-109.
22. Kausel E. Fundamental Solutions in Elastodynamics: A Compendium. 1st ed. Cambridge University Press; 2006.
23. Borcherdt RD. Effects of local geology on ground motion near San Francisco Bay. Bulletin of the Seismological Society of America. 1970;60(1):29-61.
24. Kramer SL. Geotechnical Earthquake Engineering. Prentice Hall; 1996.
25. Yuan Y, Li S, Yu H, Xiao M, Li R, Li R. Local site effect of soil-rock ground: 1-g shaking table test. Bulletin of Earthquake Engineering. 2023;21(7):3251-3272.
26. Arulanandan K. Verification of numerical procedures for the analysis of soil liquefaction problems. In: Conference Proceedings. Vol 2. Balkema; 1994.
27. Kutter BL, Carey TJ, Hashimoto T, et al. LEAP-GWU-2015 experiment specifications, results, and comparisons. Soil Dynamics and Earthquake Engineering. 2018;113:616-628.
28. Miranda G, Nappa V, Bilotta E, Haigh SK, Madabhushi GS. Physical modelling of the interaction between a tunnel and a building in a liquefying ground and its mitigation. Tunnelling and Underground Space Technology. 2023;137:105108.
29. Seed HB. Ground Motions and Soil Liquefaction during Earthquakes. Earthquake engineering research institute; 1982.
30. Fan Z, Yuan Y, Cudmani R, et al. Large biaxial laminar shear box for 1-g shaking table tests on saturated sand. Soil Dynamics and Earthquake Engineering. 2024;183:108756.

31. Wang WL, Wang TT, Su JJ, Lin CH, Seng CR, Huang TH. Assessment of damage in mountain tunnels due to the Taiwan Chi-Chi Earthquake. Tunnelling and Underground Space Technology. 2001;16(3):133-150.
32. Yashiro K, Kojima Y, Shimizu M. Historical earthquake damage to tunnels in Japan and case studies of railway tunnels in the 2004 Niigataken-Chuetsu earthquake. Quarterly Report of RTRI. 2007;48(3):136-141.
33. Yu H tao, Chen J tao, Yuan Y, Zhao X. Seismic damage of mountain tunnels during the 5.12 Wenchuan earthquake. Journal of Mountain Science. 2016;13:1958-1972.
34. Zhang X, Jiang Y, Sugimoto S. Seismic damage assessment of mountain tunnel: A case study on the Tawarayama tunnel due to the 2016 Kumamoto Earthquake. Tunnelling and underground space technology. 2018;71:138-148.
35. Chen P, Geng P, Chen J, Gu W. The seismic damage mechanism of Daliang tunnel by fault dislocation during the 2022 Menyuan Ms6.9 earthquake based on unidirectional velocity pulse input. Engineering Failure Analysis. 2023;145:107047.
36. Çetin KÖ, Ilgaç M, Can G, Çakır E. Preliminary Reconnaissance Report on February 6, 2023, Pazarcık Mw=7.7 and Elbistan Mw=7.6, Kahramanmaraş-Türkiye Earthquakes. Middle East Technical University; 2023.
37. Kiani M, Ghalandarzadeh A, Akhlaghi T, Ahmadi M. Experimental evaluation of vulnerability for urban segmental tunnels subjected to normal surface faulting. Soil Dynamics and Earthquake Engineering. 2016;89:28-37.
38. Zaheri M, Ranjbarnia M, Dias D, Oreste P. Performance of segmental and shotcrete linings in shallow tunnels crossing a transverse strike-slip faulting. Transportation Geotechnics. 2020;23:100333.
39. Zhong Z, Wang Z, Zhao M, Du X. Structural damage assessment of mountain tunnels in fault fracture zone subjected to multiple strike-slip fault movement. Tunnelling and Underground Space Technology. 2020;104:103527.
40. Ardeshiri-Lajimi S, Yazdani M, Langroudi AA. Control of fault lay-out on seismic design of large underground caverns. Tunnelling and Underground Space Technology. 2015;50:305-316.
41. Huang J, Zhao M, Du X. Non-linear seismic responses of tunnels within normal fault ground under obliquely incident P waves. Tunnelling and Underground Space Technology. 2017;61:26-39.
42. Zhou H, He C, Wang S, Peng F, Zhu S, Yuan D. Dynamic stress concentration factors and damage mode of horseshoe tunnels crossing fault fracture zone. Geotechnical and Geological Engineering. 2020;38(5):5127-5141.
43. Li R, Yuan Y, Zhao X, Bilotta E, Huang J. Local Site Effect of Fault Site and Its Impact on Seismic Response of Fault-Crossing Tunnel. Journal of Earthquake Engineering. 2024;28(11):3019-3037.
44. Zhao X, Li R, Yuan Y, Yu H, Zhao M, Huang J. Shaking table tests on fault-crossing tunnels and aseismic effect of grouting. Tunnelling and Underground Space Technology. 2022;125:104511.
45. Li R, Zhao X, Bilotta E, et al. Shaking table tests on deformation pattern and failure mechanism of fault-crossing tunnels in non-rupture scenario. Soil Dynamics and Earthquake Engineering. 2024;180:108621.